Open access • Journal Article • DOI:10.1103/PHYSREVA.75.023814

Mode coupling and cavity–quantum-dot interactions in a fiber-coupled microdisk cavity

Kartik Srinivasan, Oskar Painter

Institutions: California Institute of Technology

Published on: 23 Feb 2007 - Physical Review A (American Physical Society)

Topics: Cavity quantum electrodynamics, Mode coupling, Dephasing, Photon antibunching and Standing wave

Mode coupling and cavity–quantum-dot interactions in a fiber-coupled microdisk cavity

Kartik Srinivasan[1,*] and Oskar Painter[2]
[1]*Center for the Physics of Information, California Institute of Technology, Pasadena, California 91125, USA*
[2]*Department of Applied Physics, California Institute of Technology, Pasadena, California 91125, USA*
(Received 13 September 2006; revised manuscript received 4 December 2006; published 23 February 2007)

A quantum master equation model for the interaction between a two-level system and whispering-gallery modes (WGMs) of a microdisk cavity is presented, with specific attention paid to current experiments involving a semiconductor quantum dot (QD) embedded in a fiber-coupled $Al_xGa_{1-x}As$ microdisk cavity. In standard single mode cavity QED, three important rates characterize the system: the QD-cavity coupling rate g, the cavity decay rate κ, and the QD dephasing rate $\gamma_\perp$. A more accurate model of the microdisk cavity includes two additional features. The first is a second cavity mode that can couple to the QD, which for an ideal microdisk corresponds to a traveling wave WGM propagating counter to the first WGM. The second feature is a coupling between these two traveling wave WGMs, at a rate β, due to backscattering caused by surface roughness that is present in fabricated devices. We consider the transmitted and reflected signals from the cavity for different parameter regimes of $\{g,\beta,\kappa,\gamma_\perp\}$. A result of this analysis is that even in the presence of negligible roughness-induced backscattering, a strongly coupled QD mediates coupling between the traveling wave WGMs, resulting in an enhanced effective coherent coupling rate $g=\sqrt{2}g_0$ corresponding to that of a standing wave WGM with an electric field maximum at the position of the QD. In addition, analysis of the second-order correlation function of the reflected signal from the cavity indicates that regions of strong photon antibunching or bunching may be present depending upon the strength of coupling of the QD to each of the cavity modes. Such intensity correlation information will likely be valuable in interpreting experimental measurements of a strongly coupled QD to a bimodal WGM cavity.

DOI: 10.1103/PhysRevA.75.023814 PACS number(s): 42.50.Pq, 42.60.Da

I. INTRODUCTION

Recent demonstrations of vacuum Rabi splitting in systems consisting of a semiconductor microcavity and a single quantum dot (QD) [1–3] represent an important milestone in investigations of cavity QED in solid-state materials. In these experiments, the microcavity-QD system is incoherently pumped with an excitation beam at an energy above the bandgap of both the QD and surrounding semiconductor material (usually GaAs or some form of its alloy $Al_xGa_{1-x}As$). This pump light is absorbed and generates carriers in the GaAs system that can eventually (through phonon and carrier scattering) fill the states of the QD; under weak enough pumping conditions, only the lowest energy bound exciton state of the QD is appreciably populated on average. Radiative recombination of the exciton state and the resulting spontaneous emission is then modified by the presence of a resonant microcavity. When the cavity is of small enough volume, the coupling (g) between the QD exciton and the cavity can be large, and if the cavity decay rate κ and QD dephasing rate $\gamma_\perp$ are smaller than g, the system is said to be strongly coupled [4], in that the QD exciton and cavity mode are no longer truly separate entities but are instead bound together. In the experiments described in Refs. [1–3], the evidence of this strong coupling has been presented in the form of spontaneous emission measurements from the QD-microcavity system, which display a double-peaked structure, rather than the single peak associated with either the cavity mode or QD exciton alone. This vacuum Rabi splitting [5,6] is one signature of the strong coupling regime in cavity QED.

Applications of strongly coupled QD-microcavity systems to areas such as nonlinear optics and quantum information science [7–11] will also require an ability to effectively couple light into and out of the microcavity-QD device. That is, rather than measuring the spontaneous emission of the system alone, it is also important to have access to the cavity's optical response (transmission or reflection). This is true if, for example, one wants to examine the effect of a coupled QD-cavity system on the propagation of a subsequent beam through the cavity [7,12], or if one wants to use the phase of the emerging transmitted signal within some type of logic gate [13]. Indeed, in most cavity QED experiments involving an atom coupled to a Fabry-Perot cavity, it is the cavity's transmitted or reflected signal that is typically observed [14–17].

Following demonstrations of coupling to silica-based cavities such as microspheres [18,19] and microtoroids [20], we have recently shown that optical fiber tapers [18,21] are an effective means to couple light into and out of wavelength-scale semiconductor microcavities such as photonic crystals [22,23] and microdisks [24,25]. In addition, we have shown that microdisk cavities are extremely promising candidates for semiconductor cavity QED experiments, with recent demonstrations of cavity quality factors (Q's) in excess of 10^5 [25,26] for devices with a mode volume (V_{eff}) of $\sim 2-6(\lambda/n)^3$. These Q values are significantly larger than those utilized in Refs. [1–3], and as a result, the devices that we consider are poised to operate well within the strong coupling regime, where multiple coherent interactions between the QD and photon can occur. It is envisioned that initial

*Electronic address: kartik@caltech.edu

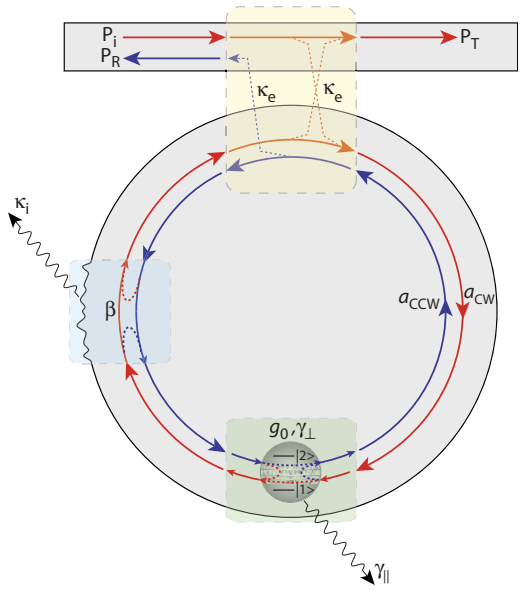

FIG. 1. (Color online) Illustration of the system under investigation. The microcavity–quantum-dot system is driven near resonance by coupling light into and out of it using an optical fiber taper waveguide, with a cavity-waveguide coupling rate κ_e (κ_e is a field amplitude decay rate). Imperfections in the microdisk cause a coupling of the clockwise and counterclockwise whispering-gallery modes, at a rate β. These two whispering-gallery modes have a quantum-dot-cavity coupling rate g_0 and intrinsic cavity decay rate κ_i. The quantum dot, approximated as a two-level system, has a radiative decay rate $\gamma_\parallel$ and a total transverse decay rate $\gamma_\perp$.

experiments in this fiber-coupled microcavity-QD system will examine vacuum-Rabi splitting through measurements of the transmission spectrum past the cavity; such measurements will be directly analogous to recent measurements of vacuum Rabi splitting from one-and-the-same atom in a Fabry-Perot cavity [17].

The goal of this paper is to provide a theoretical basis, accompanied by numerical simulations, for the experiments to be performed with single QDs in fiber-coupled microdisk cavities. Of particular concern is the proper treatment of the whispering-gallery modes (WGMs) in the cavities. More specifically, the WGMs have a degeneracy of two as modes with azimuthal number $\pm m$ have the same frequency, but circulate around the disk in opposite directions. The WGMs are typically excited through an external waveguide, and for a nearly phase-matched system the forward propagating mode through the waveguide excites only the copropagating mode in the resonator [the clockwise (CW) traveling wave WGM from here on out]. Imperfections in the resonator will change this, as they cause backscattering that can couple the CW and counterclockwise (CCW) propagating modes (Fig. 1) [24,27–30]. If the loss rates in the system (due to material absorption, scattering loss, etc.) are low enough, the backscattering can lead to coherent coupling of the CW and CCW modes, producing a pair of standing wave modes. A similar theoretical model focused on cooled alkali atoms coupled to dielectric whispering-gallery-mode microcavities has been presented by Rosenblit *et al.* in Ref. [31], and more recently by Aoki *et al.* in Ref. [32]. In this work our interest is to study this system in a parameter regime relevant to experiments involving the interaction of a single self-assembled semiconductor quantum dot with the microdisk WGMs in the presence of roughness-induced backscattering [33], and to determine the spectral response of the system for varying degrees of quantum-dot-cavity coupling (g_0), backscattering (β), and modal loss (κ_T). We examine how the phase and magnitude of the backscattering parameter affect the coupling between one or both cavity modes and the QD, and how the QD itself serves to couple the cavity modes together resulting in an enhanced coherent coupling rate over that of traveling wave WGMs.

The organization of this paper is as follows. In Sec. II, we review the simple classical coupled mode theory for modal coupling in microdisk cavities in absence of a QD. Section III presents the quantum mechanical analysis of this system in the presence of a QD. We review the quantum master equation for this system and look at semiclassical approximations for specific choices of the backscattering parameter. In Sec. IV, we present the results of numerical solutions of the quantum master equation for parameters that are accessible in current experiments. Finally, the intensity correlations in the reflected cavity signal for various parameter regimes are studied in Sec. V.

II. MODAL COUPLING OF TWO WHISPERING-GALLERY MODES DUE TO SURFACE SCATTERING

The modal coupling between CW and CCW traveling wave modes in a whispering-gallery-mode microcavity has been observed experimentally and explained by many other authors, including those of Refs. [24,27–29,34]. Here, we present a simple analysis of this coupling. This analysis is essentially an abridged version of that which appears in a recent paper by Borselli *et al.* in Ref. [30].

Maxwell's wave equation for the vector electric field in a microdisk structure is

$$\nabla^2\mathbf{E} - \mu_0(\varepsilon^0 + \delta\varepsilon)\frac{\partial^2\mathbf{E}}{\partial t^2} = 0, \tag{1}$$

where μ_0 is the permeability of free space, ϵ^0 is the dielectric function for the ideal (perfectly cylindrical) microdisk, and $\delta\epsilon$ is the dielectric perturbation that is the source of mode coupling between the CW and CCW modes. Assuming a harmonic time dependence, the complex field modes of the ideal ($\delta\epsilon=0$) microdisk structure can be written as $\mathbf{E}_j^0(\mathbf{r},t)=\mathbf{E}_j^0(\mathbf{r})\exp(i\omega_j t)$, where j is an index label including the azimuthal number (m), radial order (p), vertical order (v), and vertical parity (odd or even for a cylinder with mirror symmetry). In the microdisk structures of interest the vertical height of the dielectric cylinder is typically a half wavelength in thickness, and only the lowest order vertical mode is well localized to the microdisk. In this case the vertical order and parity can be combined to define the fundamental vertically guided whispering-gallery modes of the disk as transverse electric (TE), with antinode of the in-plane $(\hat{\rho},\hat{\phi})$ electric field components at the center height of the disk, and transverse magnetic (TM), with antinode of the

vertical ($\hat{z}$) electric field component at the center height of the disk. In what follows we will continue to use the TE and TM designation when discussing the WGMs, however, it should be noted that due to the radial guiding of the modes in the small microdisks of interest to this work the WGMs are far from actually transverse electric or magnetic, and contain significant longitudinal field components in the azimuthal direction.

Solutions to Eq. (1) with $\delta\epsilon \neq 0$ (i.e., modes of the perturbed structure) are written as a sum of the unperturbed mode basis

$$\mathbf{E}(\mathbf{r},t) = e^{-i\omega_0 t}\sum_j a_j(t)\mathbf{E}_j^0(\mathbf{r}). \tag{2}$$

Plugging into Eq. (1), keeping only terms up to first order, and utilizing mode orthogonality, we arrive at a set of coupled mode equations

$$\frac{da_k}{dt} + i\Delta\omega_k a_k(t) = i\sum_j \beta_{jk} a_j(t), \tag{3}$$

$$\beta_{jk} = \frac{\omega_0}{2}\frac{\int \delta\epsilon[\mathbf{E}_j^0(\mathbf{r})]^* \cdot \mathbf{E}_k^0(\mathbf{r})d\mathbf{r}}{\int \epsilon^0|\mathbf{E}_k^0(\mathbf{r})|^2 d\mathbf{r}}. \tag{4}$$

Reference [30] presents a functional form for β in situations involving small surface roughness perturbation. Under weak scattering conditions an assumption is made that only each pair (common radial order, etc.) of localized, degenerate CW and CCW WGMs with azimuthal mode number $\pm m$ are coupled by the disk perturbation $\delta\epsilon$. The complex electric fields of the CW and CCW WGMs are simply related [35], and can be written in a cylindrical (ρ,ϕ,z) coordinate system as

$$\mathbf{E}_{\mathrm{CW}}^0(\mathbf{r}) = [E_\rho^0(\rho,z), iE_\phi^0(\rho,z), E_z^0(\rho,z)]e^{im\phi},$$

$$\mathbf{E}_{\mathrm{CCW}}^0(\mathbf{r}) = [E_\rho^0(\rho,z), -iE_\phi^0(\rho,z), E_z^0(\rho,z)]e^{-im\phi}. \tag{5}$$

In the case of high-Q resonant modes, with a small degree of loss per round-trip, the CW and CCW WGMs are to a good approximation complex conjugates of each other, which when combined with Eq. (5) indicate that the WGMs can be written with transverse $(\hat{\rho},\hat{z})$ electric field components real and longitudinal $(\hat{\phi})$ components imaginary [35] (i.e., $E_\rho^0, E_\phi^0, E_z^0$ all real functions). The coupled mode equations for these traveling wave modes then read

$$\frac{da_{\mathrm{CW}}}{dt} = -i\Delta\omega a_{\mathrm{CW}}(t) + i|\beta|e^{i\xi}a_{\mathrm{CCW}}(t),$$

$$\frac{da_{\mathrm{CCW}}}{dt} = -i\Delta\omega a_{\mathrm{CCW}}(t) + i|\beta|e^{-i\xi}a_{\mathrm{CW}}(t), \tag{6}$$

with $\beta = |\beta|e^{i\xi}$ given by (in a basis with the transverse electric field components of the WGMs real),

$$\beta = \frac{\omega_0}{2}\frac{\int\left(\int \delta\epsilon e^{+i2m\phi}d\phi\right)[(\mathbf{E}_\rho^0)^2 - (\mathbf{E}_\phi^0)^2 + (\mathbf{E}_z^0)^2]\rho d\rho dz}{2\pi\int \epsilon^0[(\mathbf{E}_\rho^0)^2 + (\mathbf{E}_\phi^0)^2 + (\mathbf{E}_z^0)^2]\rho d\rho dz}. \tag{7}$$

Equation (6) represents the time evolution of the two mode amplitudes $(a_{\mathrm{CW}}, a_{\mathrm{CCW}})$ of an isolated system, without loss or coupling to an external waveguide. For the experiments considered in our work, the waveguide coupler will be an optical fiber taper through which light is traveling in the forward propagating mode. Light coupled from the fiber taper will selectively excite the clockwise WGM of the microdisk structure due to phase matching. Following the formalism of Ref. [36] this waveguide-resonator coupling can be included through the addition of a term ks_+ to Eq. (6), where k is a waveguide coupling coefficient and $|s_+|^2$ is the input *power* in the external waveguide (the squared magnitude of the mode amplitudes $|a_{\mathrm{CW,CCW}}|^2$ are normalized to stored optical *energy* in the cavity). Loss is introduced to the coupled mode equations by use of the phenomenological field *amplitude* decay rate κ_T, taken to be the same for both the CW and CCW modes (though in general this does not have to be the case). This total field decay rate is broken into a contribution from intrinsic microdisk absorption and scattering loss (κ_i) and a contribution due to coupling to the external waveguide (κ_e), so that $\kappa_T = \kappa_i + \kappa_e$. Assuming lossless coupling and time reversal symmetry it can be shown [36] that $|k|^2 = 2\kappa_e$. The coupled mode equations then read

$$\frac{da_{\mathrm{CW}}}{dt} = -(\kappa_T + i\Delta\omega)a_{\mathrm{CW}}(t) + i|\beta|e^{i\xi}a_{\mathrm{CCW}}(t) + t(i\sqrt{2\kappa_e})s_+,$$

$$\frac{da_{\mathrm{CCW}}}{dt} = -(\kappa_T + i\Delta\omega)a_{\mathrm{CCW}}(t) + i|\beta|e^{-i\xi}a_{\mathrm{CW}}(t). \tag{8}$$

Here, the phase of the coupling coefficient was (arbitrarily) chosen to be purely imaginary, corresponding to a single-pass, waveguide transmission coefficient of +1 in the lossless coupler case [36]. These two coupled equations can be rewritten as uncoupled equations in terms of the variables $a_{\mathrm{SW},1}$ and $a_{\mathrm{SW},2}$, which represent the standing wave mode amplitudes

$$a_{\mathrm{SW},1} = \frac{1}{\sqrt{2}}(a_{\mathrm{CW}} + e^{i\xi}a_{\mathrm{CCW}})$$

$$a_{\mathrm{SW},2} = \frac{1}{\sqrt{2}}(a_{\mathrm{CW}} - e^{i\xi}a_{\mathrm{CCW}}). \tag{9}$$

As mentioned above, for an ideal microdisk the field distributions of mode amplitudes a_{CW} and a_{CCW} have an azimuthal spatial dependence of $e^{\pm im\phi}$, so that the field distributions of $a_{\mathrm{SW},1}$ and $a_{\mathrm{SW},2}$ correspond to (up to an overall phase factor) standing waves $\sqrt{2}\cos(m\phi - \xi/2)$ and $\sqrt{2}\sin(m\phi - \xi/2)$, respectively, with the azimuthal orientation of the standing waves being determined by the phase ξ of the backscattering parameter. Here, and in what follows, we take the

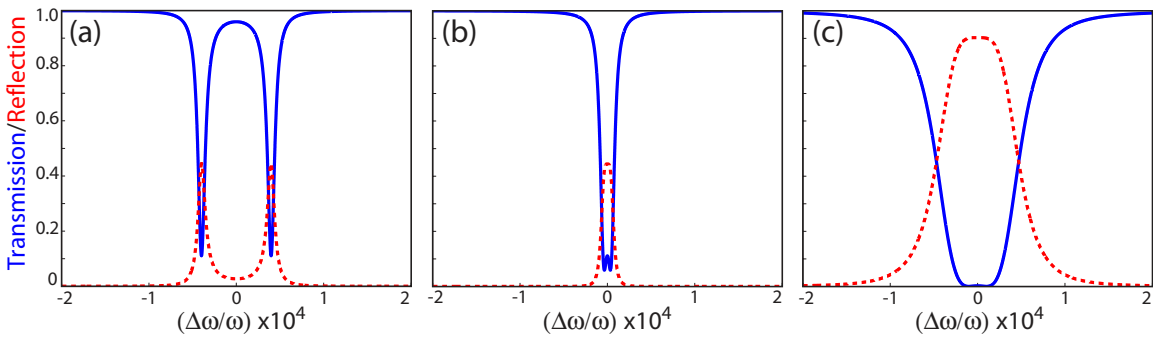

FIG. 2. (Color online) Normalized transmitted (solid line) and reflected (dashed line) signal for standing wave whispering-gallery modes, determined through steady state solution of the coupled mode equations given in Eq. (8). (a) $\beta/\kappa_T=8$, $\kappa_T/\kappa_i=3$ (b) $\beta/\kappa_T=1$, $\kappa_T/\kappa_i=3$, and (c) $\beta/\kappa_T=1$, $\kappa_T/\kappa_i=20$. $Q_i=3\times10^5$ in all cases.

origin of the azimuthal axis ($\phi=0$) to be centered at the QD.

The transmitted (P_T) and reflected (P_R) optical power in the external waveguide can be determined in either the basis of ($a_{\mathrm{CW}}, a_{\mathrm{CCW}}$) or ($a_{\mathrm{SW},1}, a_{\mathrm{SW},2}$); because of phase matching, coupling between the external waveguide and WGM resonator occur directly through ($a_{\mathrm{CW}}, a_{\mathrm{CCW}}$) and it is most natural to solve for these quantities in the traveling wave mode basis. With the phase of the coupling coefficient chosen as purely imaginary the transmitted and reflected powers are $P_T=|s_+ + (i\sqrt{2\kappa_e})a_{\mathrm{CW}}|^2$ and $P_R=|(i\sqrt{2\kappa_e})a_{\mathrm{CCW}}|^2$, respectively. Steady state solutions for the normalized transmitted and reflected signals from the cavity for a number of different parameters are shown in Fig. 2. For $\beta>\kappa_T$ [Fig. 2(a)], we see the formation of a distinct pair of resonances, located at $\omega\approx\omega_0\pm\beta$. These dips correspond to standing wave resonances that result from a backscattering rate (β) that exceeds all other losses in the system (κ_T) so that coherent coupling between the CW and CCW modes can take place. As we see in Figs. 2(b) and 2(c), for $\beta\sim\kappa_T$, the resonances begin to overlap and are no longer distinguishable.

For cavity QED applications, one very important consequence of the distinction between traveling wave and standing wave modes is in the effective volume of the mode (V_{eff}), as the peak electric field strength per photon in the cavity scales as $1/\sqrt{V_{\mathrm{eff}}}$. In particular, we recall the definition of V_{eff} as

$$V_{\mathrm{eff}}=\frac{\int \epsilon|\mathbf{E}(\mathbf{r})|^2}{\max[\epsilon|\mathbf{E}(\mathbf{r})|^2]}. \tag{10}$$

Standing wave WGMs have approximately half the volume of the traveling wave WGMs, so that the coupling rate g between a single quantum dot and a single photon in a standing wave cavity mode is expected to be $\sqrt{2}$ times that when the quantum dot is coupled to a traveling wave cavity mode. This of course assumes the single QD is positioned at an antinode of the standing wave mode; alternately, if it happens to be positioned at a node, the coupling rate g will be zero.

These arguments again rely upon having a physical system in which the backscattering coupling between CW and CCW modes is sufficiently strong compared to all other loss rates to allow for coherent modal coupling and formation of standing waves. They have also neglected the effects that an embedded QD may have, due to both an introduction of additional loss and mode coupling into the system. In the case of a strongly coupled QD we might expect that standing wave modes can be maintained provided that the modal coupling rate β exceeds not only κ_T but also the QD spontaneous emission rate $\gamma_{\|}$ and nonradiative dephasing rate γ_p. To verify our physical intuition and understand the system in better detail, we consider a quantum master equation approach [37] to take into account the cavity-QD interaction.

III. QUANTUM MASTER EQUATION MODEL

We begin by considering the Hamiltonian for an empty microdisk cavity (traveling wave WGM resonance frequency ω_c) with field operators $\hat{a}_{\mathrm{CW}}$ and $\hat{a}_{\mathrm{CCW}}$ and mode coupling parameter β, written in a frame rotating at the driving frequency ω_l (and for $\hbar=1$):

$$H_0=\Delta\omega_{cl}\hat{a}^\dagger_{\mathrm{CW}}\hat{a}_{\mathrm{CW}}+\Delta\omega_{cl}\hat{a}^\dagger_{\mathrm{CCW}}\hat{a}_{\mathrm{CCW}}-\beta\hat{a}^\dagger_{\mathrm{CW}}\hat{a}_{\mathrm{CCW}} - \beta^*\hat{a}^\dagger_{\mathrm{CCW}}\hat{a}_{\mathrm{CW}}+i(E\hat{a}^\dagger_{\mathrm{CW}}-E^*\hat{a}_{\mathrm{CW}}), \tag{11}$$

where $\Delta\omega_{cl}=\omega_c-\omega_l$. As in the coupled-mode equations of the previous section, the CW propagating mode is driven by a classical intracavity field $E=i\sqrt{2\kappa_e P_{\mathrm{in}}}$, where κ_e is the cavity field decay rate into the waveguide and P_{in} is the input power in the external waveguide. From this Hamiltonian, the classical coupled-mode equations without dissipation can easily be derived through an application of Ehrenfest's theorem.

Modeling the QD as a two-level system, we add the term H_1 to the Hamiltonian

$$H_1=\Delta\omega_{al}\hat{\sigma}_+\hat{\sigma}_- + ig_0(\hat{a}^\dagger_{\mathrm{CW}}\hat{\sigma}_- - \hat{a}_{\mathrm{CW}}\hat{\sigma}_+) + ig_0(\hat{a}^\dagger_{\mathrm{CCW}}\hat{\sigma}_- - \hat{a}_{\mathrm{CCW}}\hat{\sigma}_+), \tag{12}$$

where $\Delta\omega_{al}=\omega_a-\omega_l$, ω_a is the transition frequency of the exciton state of the QD, and g_0 is the coherent coupling strength between the QD exciton state and the traveling wave WGMs. Note that g_0 has been assumed real, and to have the same phase for both CW and CCW WGMs in Eq. (12). This is consistent with a choice of the azimuthal origin lying at the location of the QD and for a QD dipole polarization transverse to the $\hat{\phi}$ direction, where the electric field compo-

nents for both WGMs are equal and real at the position of the QD (a WGM basis can also be chosen in which this is true for dipole polarization parallel to $\hat{\phi}$). For a QD located away from the azimuthal zero or with a mixed transverse and parallel dipole orientation, g_0 will be complex, having a different phase for the CW and CCW modes. In general, care must be taken to calculate g_0 and β consistently when studying interference effects between QD dipole scattering and roughness-induced scattering.

The equation of motion for the system's density matrix ρ can be found from the equation

$$\frac{d\rho}{dt} = \frac{1}{i}[H_0 + H_1, \rho] + L\rho, \tag{13}$$

where the term $L\rho=(L_1+L_2+L_3)\rho$ allows for the inclusion of decay through cavity loss (at a rate $\kappa_T=\omega_c/2Q$), quantum dot spontaneous emission (at a rate $\gamma_\parallel$), and phase-destroying collisional processes (at a rate γ_p), which are of particular importance for quantum dots, as unlike atoms, they are embedded in a semiconductor matrix where electron-phonon scattering is non-negligible. In the zero-temperature limit (applicable to the experiments under consideration as they will occur at cryogenic temperatures), these loss terms are given by [37,38]

$$L_1\rho = \kappa_T(2\hat{a}_{\mathrm{CW}}\rho\hat{a}_{\mathrm{CW}}^\dagger - \hat{a}_{\mathrm{CW}}^\dagger\hat{a}_{\mathrm{CW}}\rho - \rho\hat{a}_{\mathrm{CW}}^\dagger\hat{a}_{\mathrm{CW}}) + \kappa_T(2\hat{a}_{\mathrm{CCW}}\rho\hat{a}_{\mathrm{CCW}}^\dagger - \hat{a}_{\mathrm{CCW}}^\dagger\hat{a}_{\mathrm{CCW}}\rho - \rho\hat{a}_{\mathrm{CCW}}^\dagger\hat{a}_{\mathrm{CCW}}), \tag{14}$$

$$L_2\rho = \frac{\gamma_\parallel}{2}(2\hat{\sigma}_-\rho\hat{\sigma}_+ - \hat{\sigma}_+\hat{\sigma}_-\rho - \rho\hat{\sigma}_+\hat{\sigma}_-), \tag{15}$$

$$L_3\rho = \frac{\gamma_p}{2}(\hat{\sigma}_z\rho\hat{\sigma}_z - \rho). \tag{16}$$

From the master equation, we can numerically calculate the steady state density matrix ρ_{SS} and relevant operator expectation values such as $\langle\hat{a}_{\mathrm{CW}}^\dagger\hat{a}_{\mathrm{CW}}\rangle_{\mathrm{SS}}$, which will then allow us to determine the transmission and reflection spectrum of the coupled QD-cavity system using formulas that are analogous to those used in the classical model of Sec. II. These calculations are the subject of the following section. For now, however, we consider what intuition may be gained by further analytical study of the master equation. Using the standing wave mode operators

$$\hat{a}_{\mathrm{SW},1} = \frac{1}{\sqrt{2}}(\hat{a}_{\mathrm{CW}} + e^{i\xi}\hat{a}_{\mathrm{CCW}})$$

$$\hat{a}_{\mathrm{SW},2} = \frac{1}{\sqrt{2}}(\hat{a}_{\mathrm{CW}} - e^{i\xi}\hat{a}_{\mathrm{CCW}}) \tag{17}$$

and writing $\beta=|\beta|e^{i\xi}$, we take operator expectation values to arrive at

$$\frac{d}{dt}\langle\hat{a}_{\mathrm{SW},1}\rangle = -i(\Delta\omega_{cl} - |\beta|)\langle\hat{a}_{\mathrm{SW},1}\rangle + g_0\frac{1+e^{i\xi}}{\sqrt{2}}\langle\hat{\sigma}_-\rangle - \kappa_T\langle\hat{a}_{\mathrm{SW},1}\rangle + \frac{E}{\sqrt{2}},$$

$$\frac{d}{dt}\langle\hat{a}_{\mathrm{SW},2}\rangle = -i(\Delta\omega_{cl} + |\beta|)\langle\hat{a}_{\mathrm{SW},2}\rangle + g_0\frac{1-e^{i\xi}}{\sqrt{2}}\langle\hat{\sigma}_-\rangle - \kappa_T\langle\hat{a}_{\mathrm{SW},2}\rangle + \frac{E}{\sqrt{2}},$$

$$\frac{d}{dt}\langle\hat{\sigma}_-\rangle = -(i\Delta\omega_{al} + \gamma_\perp)\langle\hat{\sigma}_-\rangle + \frac{g_0}{\sqrt{2}} \times[\langle\hat{\sigma}_z\hat{a}_{\mathrm{SW},1}\rangle(1+e^{-i\xi}) + \langle\hat{\sigma}_z\hat{a}_{\mathrm{SW},2}\rangle(1-e^{-i\xi})]$$

$$\frac{d}{dt}\langle\hat{\sigma}_z\rangle = -\sqrt{2}g_0[\langle\hat{\sigma}_-\hat{a}_{\mathrm{SW},1}^\dagger\rangle(1+e^{i\xi}) + \langle\hat{\sigma}_-\hat{a}_{\mathrm{SW},2}^\dagger\rangle(1-e^{i\xi})] - \sqrt{2}g_0[\langle\hat{\sigma}_+\hat{a}_{\mathrm{SW},1}\rangle(1+e^{-i\xi}) + \langle\hat{\sigma}_+\hat{a}_{\mathrm{SW},2}\rangle(1-e^{-i\xi})] - \gamma_\parallel(1+\langle\hat{\sigma}_z\rangle), \tag{18}$$

where we have used $[\hat{\sigma}_+,\hat{\sigma}_-]=\hat{\sigma}_z$ and $\gamma_\perp=\gamma_\parallel/2+\gamma_p$. In the new standing wave mode basis both the empty-cavity frequencies and the QD-cavity coupling strengths are seen to be modified by the presence of strong backscattering. For the low-frequency mode $(\omega_c-|\beta|)$ corresponding to field operator $\hat{a}_{\mathrm{SW},1}$, the effective coupling strength is $g_{\mathrm{SW},1}=g_0(1+e^{i\xi})/\sqrt{2}$, while for the high-frequency mode $(\omega_c+|\beta|)$ corresponding to field operator $\hat{a}_{\mathrm{SW},2}$, the effective coupling strength is $g_{\mathrm{SW},2}=g_0(1-e^{i\xi})/\sqrt{2}$. These coupling strengths are thus dependent on the phase ξ of the backscattering parameter β and can be as large as $\sqrt{2}g_0$ or as small as zero. This result is consistent with what one would expect intuitively; the superposition of traveling wave modes results in a pair of standing wave modes whose peak field strength (per photon) is $\sqrt{2}$ times that of a traveling wave mode. The two standing wave modes are phase shifted from each other in the azimuthal direction by $\pi/2$, and as a result, if the QD is positioned in the antinode of one mode ($\xi=0$, so that $g_{\mathrm{SW},1}=\sqrt{2}g_0$), it is within a node of the other mode (so that $g_{\mathrm{SW},2}=0$), and vice versa for the situation when $\xi=\pi$. Of course, for large cooperativity, C, between the traveling wave cavity modes and the QD, the modes $(\hat{a}_{\mathrm{SW},1},\hat{a}_{\mathrm{SW},2})$ may no longer be a good eigenbasis of the system. In order to gain some insight into such situations before moving on to numerical quantum master equation simulations, we consider below steady state solutions to the semiclassical equations.

The semiclassical equations of motion, derived from the above equations by assuming that expectation values of products of operators equal the product of the expectation values, can be solved in steady state to yield information about the cavity response as a function of drive strength and detunings, and are useful for understanding the linear and

nonlinear spectroscopy of the system [9,11,39–41]. In the case of a single cavity mode coupled to a two-level system this leads to the standard optical bistability state equation (OBSE). We consider two examples from the microdisk model described above with two cavity modes, one in which the scattering by the QD and the roughness-induced backscattering are in phase and the coupling between the QD and cavity mode are described by the simple intuitive picture above, the other in which the two processes compete and the system response is more complicated. We begin with the simplest case in which $\xi=0$ (the $\xi=\pi$ case is identical except the roles of $\hat{a}_{\mathrm{SW},1}$ and $\hat{a}_{\mathrm{SW},2}$ are swapped). Defining the parameters

$$n_s = \frac{\gamma_\perp \gamma_\parallel}{4g_0^2}, \quad C = \frac{g_0^2}{2\kappa_T \gamma_\perp},$$

$$Y = \frac{E}{\sqrt{2n_s}\kappa_T},$$

$$X_+ = \frac{\langle \hat{a}_{SW,1}\rangle|_{\xi=0}}{\sqrt{n_s}}, \quad X_- = \frac{\langle \hat{a}_{SW,2}\rangle|_{\xi=0}}{\sqrt{n_s}}, \tag{19}$$

and solving Eq. (18) with $\xi=0$ in steady state we arrive at the following expressions relating the external drive (Y) to the internal state of the cavity (X_+, X_-):

$$X_+ = \frac{Y}{1+\dfrac{4C}{2|X_+|^2+\left(\dfrac{\Delta\omega_{al}}{\lambda_\perp}\right)^2+1}+i\left(\dfrac{\Delta\omega_{cl}-\beta}{\kappa_T}-\dfrac{4C\left(\dfrac{\Delta\omega_{al}}{\gamma_\perp}\right)}{2|X_+|^2+\left(\dfrac{\Delta\omega_{al}}{\lambda_\perp}\right)^2+1}\right)},$$

$$X_- = \frac{Y}{1+i\left(\dfrac{\Delta\omega_{cl}+\beta}{\kappa_T}\right)}. \tag{20}$$

Due to the common phase of the backscattering and the QD mode coupling in this case, the net effect of the backscattering on the system response is simply to shift the resonance frequencies of the empty-cavity modes. As expected the QD couples to one standing wave mode with a cooperativity twice that of a traveling wave mode, and is decoupled from the other.

In the general case both standing wave WGMs couple to the QD and obtaining an equation analogous to the OBSE for an arbitrary ξ is somewhat algebraically tedious. As a simple example in which both modes are coupled to the QD we consider $\xi=\pi/2$, which yields in steady state

$$X_+ = \frac{Y}{\left(\dfrac{1+i\Delta\omega_{cl}/\kappa_T}{1+i\Delta\omega_{cl}/\kappa_T+|\beta|/\kappa_T}\right)\left[1+\dfrac{(|\beta|/\kappa_T)^2}{1+\left(\dfrac{\Delta\omega_{cl}}{\kappa_T}\right)^2}+\dfrac{4C}{2X_+^2+\left(\dfrac{\Delta\omega_{al}}{\gamma_\perp}\right)^2+1}+i\left(\dfrac{\Delta\omega_{cl}}{\kappa_T}\left(1-\dfrac{(|\beta|/\kappa_T)^2}{1+\left(\dfrac{\Delta\omega_{cl}}{\kappa_T}\right)^2}\right)-\dfrac{4C\left(\dfrac{\Delta\omega_{al}}{\gamma_\perp}\right)}{2X_+^2+\left(\dfrac{\Delta\omega_{al}}{\gamma_\perp}\right)^2+1}\right)\right]},$$

$$X_- = \frac{Y-\dfrac{|\beta|}{\kappa_T}X_+}{1+i\dfrac{\Delta\omega_{cl}}{\kappa_T}}. \tag{21}$$

In this case the backscattering and the QD mode coupling are out of phase and in competition. The resulting system response is governed by the detunings $(\Delta\omega_{al}, \Delta\omega_{cl})$ and the relative magnitude of the normalized roughness-induced backscattering $(|\beta|/\kappa_T)^2$ and the cooperativity C.

Finally note that in order to connect to experiment an input-output expression between the incoming optical signal in the waveguide and the optical transmission (or reflection) past the cavity into our collection fiber is desired. In the formalism presented in Sec. II the transmission and reflection are given in terms of the traveling wave mode amplitudes. These amplitudes can easily be recovered from even and odd parity superpositions of X_+ and X_- [see Eq. (17)].

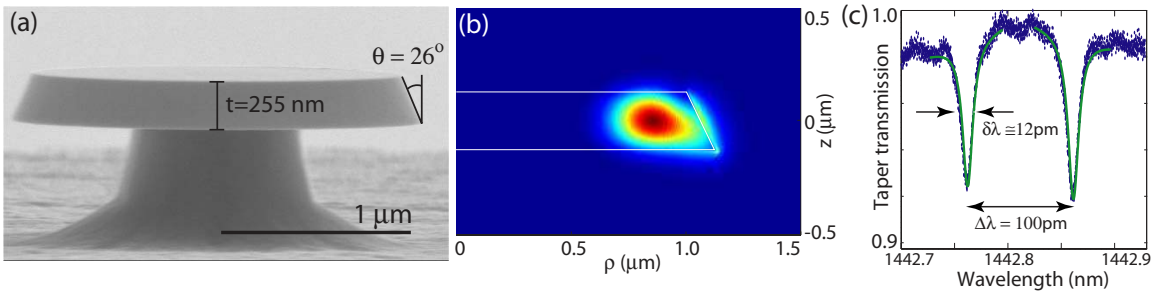

FIG. 3. (Color online) (a) Scanning electron microscope (SEM) image of a fabricated microdisk device. The disk thickness is $t=255$ nm and the sidewall angle is $\theta=26°$ from vertical. The measured average diameter for this device (i.e., the diameter at the center of the slab) is 2.12 μm. (b) Finite-element-calculated $|\mathbf{E}|^2$ distribution for the $\mathrm{TE}_{p=1,m=11}$ WGM of a microdisk with a diameter of 2.12 μm at the center of the slab. For this mode, $\lambda \sim 1265.41$ nm, $Q_{\mathrm{rad}} \sim 10^7$, and for a traveling wave mode, $V_{\mathrm{eff}} \sim 5.6(\lambda/n)^3$. (c) Typical measured normalized optical transmission spectrum of the $\mathrm{TE}_{p=1,9}$ WGMs of a 2 μm diameter microdisk similar to that in the SEM image of (a).

IV. SOLUTIONS TO THE STEADY STATE QUANTUM MASTER EQUATION IN THE WEAK DRIVING REGIME

The quantum master equation (QME) presented in the previous section is solved numerically using the Quantum Optics Toolbox [42,43]. We begin by considering steady state solutions, and calculate the transmitted and reflected optical signals from the cavity. As a starting point, we eliminate the quantum dot from the problem by taking the coupling rate $g_0=0$. As expected, the resulting solutions (not displayed here) are identical to those obtained using the classical coupled mode equations and presented in Fig. 2. Having confirmed that the QME solution is consistent with the classical solution in the empty cavity limit, we move on to study interactions with the quantum dot. To connect these simulations to ongoing experiments we choose physical parameters consistent with our fabricated devices [25,26]. In these experiments the microdisk cavity is 255 nm thick, and has a sidewall angle of 26° as shown in Fig. 3(a). The modes of these structures [Fig. 3(b)] can be numerically investigated through finite-element eigenfrequency calculations using the Comsol FEMLAB software [26,44,45], and information about the effective modal volume V_{eff} [as defined in Eq. (9)] and radiation-limited quality factor Q_{rad} can be obtained. For the purposes of this work we focus on modes of transverse electric (TE) polarization, where the electric field lies predominantly within the plane of the disk, and we consider first order radial modes ($p=1$) in the 1200 nm wavelength band, the wavelength region of the ground state exciton transition in our QDs.

As discussed in Ref. [26], finite-element method simulations can be used to calculate V_{eff} as a function of the average microdisk diameter D_{avg}. From V_{eff}, we can estimate the QD-photon coupling strength. For a QD located at a position of maximum electric field energy density and with exciton dipole parallel to the local electric field of the cavity mode $g_0=\mathbf{d}\cdot\mathbf{E}_{\mathrm{ph}}/\hbar$ is given by [4,46]

$$g_0 = \frac{1}{2\tau_{\mathrm{sp}}}\sqrt{\frac{3c\lambda_0^2\tau_{\mathrm{sp}}}{2\pi n^3 V_{\mathrm{eff}}}}, \tag{22}$$

where τ_{sp} is the spontaneous emission lifetime of the QD exciton. Consistent with what has been measured experimentally for self-assembled InAs quantum dots [47], we take $\tau_{\mathrm{sp}}=1$ ns. Figure 4 shows a plot of g_0 versus disk size for traveling wave WGMs, and we see that $g_0/2\pi$ can be as high as 16 GHz for the range of diameters we consider. As discussed in Ref. [26], the WGMs are well confined ($Q_{\mathrm{rad}}>10^5$) for all but the smallest diameter disks ($D_{\mathrm{avg}}<1.5$ μm). We have confirmed this in experiments [26,48], with Q as high as 3.6×10^5 measured, so that cavity decay rates $\kappa_T/2\pi$ of approximately 1 GHz can reasonably be expected. Such devices exhibited doublet splittings that are on the order of $\Delta\lambda=10-100$ pm [see Fig. 3(c)], corresponding to a backscattering rate $|\beta|/2\pi=1-10$ GHz. In practical devices then, the roughness-induced backscattering and the coherent QD-cavity mode coupling rates can be of similar magnitude, and we thus expect the QME simulation results to be particularly helpful in interpreting future experimental data.

Unless otherwise specified, in all of the QME simulations to follow we consider the weak driving limit. In this limit the steady state response of the system behaves linearly, with the internal cavity photon number $\ll 1$ and QD saturation effects negligible. For the QD and cavity parameters of the microdisk structures described below this corresponds to input powers of about 10 pW.

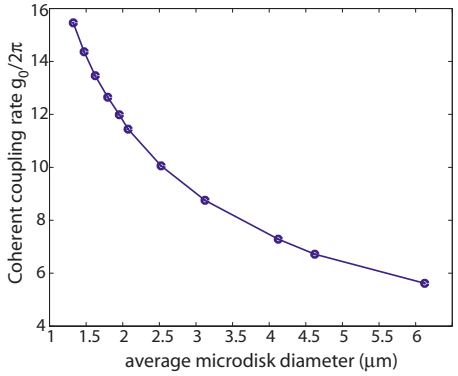

FIG. 4. (Color online) Coherent coupling rate $g_0/2\pi$ (with $\tau_{\mathrm{sp}}=1$ ns) for traveling wave $\mathrm{TE}_{p=1,m}$ whispering-gallery modes of the microdisk structure described in Fig. 3 with varying disk diameter. Calculations were performed using a fully vectorial finite-element method, where for each microdisk diameter the azimuthal number of the $\mathrm{TE}_{p=1,m}$ WGM resonance was adjusted to place the resonance frequency nearest $\lambda=1250$ nm.

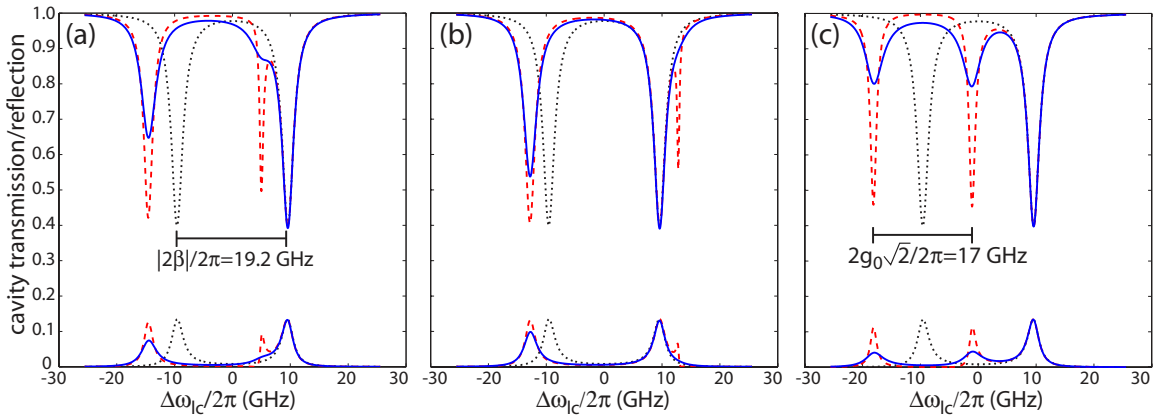

FIG. 5. (Color online) Steady state QME solution for the normalized optical transmission (top curves) and reflection (bottom curves) spectra for a QD coupled to a microdisk cavity under weak driving and for three different QD detunings: (a) $\Delta\omega_{ac}=0$, (b) $\Delta\omega_{ac}=\beta$, and (c) $\Delta\omega_{ac}=-\beta$. Cavity and QD parameters for these simulations are $\{g_0,\beta,\kappa_T,\kappa_e,\gamma_\parallel,\gamma_p\}/2\pi=\{6,9.6,1.2,0.44,0.16,2.4\}$ GHz, with the phase of the backscattering parameter set to $\xi=0$. In these plots the additional black dotted line plots correspond to an empty cavity ($g_0=0$) and the red dashed line plots correspond to a QD with no nonradiative dephasing ($\gamma_p/2\pi=0$ GHz).

A. $\beta > g_0 > (\kappa_T, \gamma_\perp)$

The first situation we study is one in which the backscattering rate β exceeds the coupling rate g_0, which in turn exceeds the cavity and QD decay rates κ_T and $\gamma_\perp$. We choose $\beta/2\pi=9.6$ GHz ($\xi=0$), with $g_0/2\pi=6$ GHz, $\kappa_T/2\pi=1.2$ GHz (corresponding to $Q=10^5$), $\kappa_e/2\pi=0.44$ GHz (corresponding to a transmission depth of 60% for the empty-cavity standing wave modes), and $\tau_{sp}=1$ ns($\gamma_\parallel/2\pi \sim 0.16$ GHz). The unperturbed cavity frequency (i.e., the resonance frequency of the *traveling wave* modes) is fixed at $\omega_c=0$, and three different QD-cavity detunings, $\Delta\omega_{ac}=\omega_a-\omega_c=\{0,\beta,-\beta\}$ are considered. For each value of $\Delta\omega_{ac}$, we calculate the steady state transmission and reflection spectra (as a function of probe laser frequency to cavity detuning, $\Delta\omega_{lc}=\omega_l-\omega_c$) from the cavity in three different limits: (i) $g_0=0$; here, there is no QD-cavity coupling, and the response should be that of an empty cavity, (ii) $g_0/2\pi=6$ GHz, $\gamma_p/2\pi=0$ GHz; here, we neglect all nonradiative dephasing, which becomes a good approximation as the temperature of the QD is cooled below 10 K, and (iii) $g_0/2\pi=6$ GHz, $\gamma_p/2\pi=2.4$ GHz; here, we allow for a significant amount of nonradiative dephasing, corresponding to a QD exciton linewidth of 10 μeV, which is consistent with what has been observed experimentally at temperatures of around 10–20K [47].

The results of the steady-state quantum master equation simulations are plotted in Fig. 5. The interpretation of these results is as follows: as a result of the modal coupling due to backscattering, which has formed standing wave modes through a superposition of the initial traveling wave modes, only the lower frequency mode of the doublet has any spatial overlap with the QD (see Fig. 6 for location of the QD relative to the two standing wave modes as a function of ξ), and thus, we should only expect the low frequency mode to exhibit any frequency shifts or splittings. In Fig. 5(a), with the QD spectrally detuned equally from both empty-cavity standing wave modes, we see *asymmetric* vacuum Rabi splitting due to coupling of the QD to the low frequency mode at $\omega_c-\beta$. In Fig. 5(b), with the QD now on resonance with the higher frequency mode, coupling still only occurs to the low frequency mode detuned in this case by 2β. Finally in Fig. 5(c), the QD is on resonance with the low frequency mode, and is also spatially aligned with it, so that we see the familiar *symmetric* vacuum Rabi splitting of this resonance. We note that the frequency splitting, Ω_R, is in this case $2\sqrt{2}g_0$

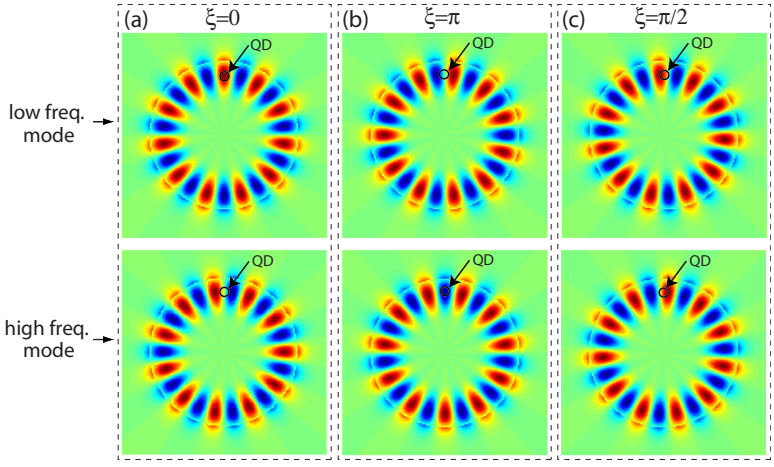

FIG. 6. (Color online) Standing wave modes in a microdisk for different phases of β showing how the low and high frequency modes are positioned with respect to a fixed QD. (a) $\beta>0$ ($\xi=0$), (b) $\beta<0$ ($\xi=\pi$), and (c) $\beta=i|\beta|$ ($\xi=\pi/2$).

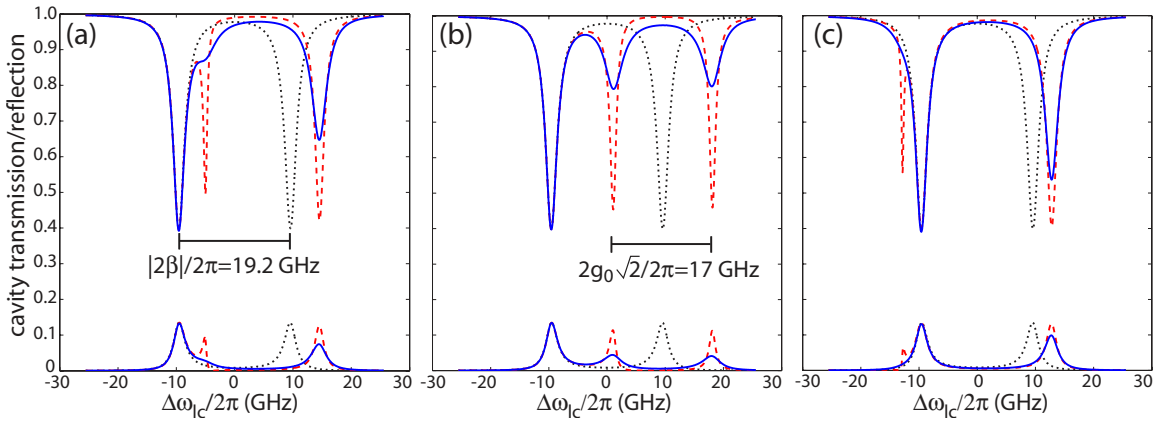

FIG. 7. (Color online) Steady state QME solution for the normalized optical transmission (top curves) and reflection (bottom curves) spectra of a QD coupled to a microdisk cavity under weak driving and for three different QD detunings: (a) $\Delta\omega_{ac}=0$, (b) $\Delta\omega_{ac}=\beta$, and (c) $\Delta\omega_{ac}=-\beta$. These plots are calculated for identical parameters as in Fig. 5 with the exception that the phase of the backscattering parameter β has been changed from $\xi=0$ to $\xi=\pi$ ($\beta/2\pi=-9.6$ GHz).

rather than $2g_0$; this is consistent with the mode volume of the standing wave modes being one half that of the traveling wave modes. For $\xi=\pi$ (Fig. 7) the results are the mirror image of those in Fig. 5, where now the high frequency mode is spatially aligned with the QD and exhibits frequency shifts and vacuum Rabi splitting.

Finally, we consider an intermediate backscattering phase $\xi=\pi/2$. Here, we expect both modes to have an equal (but nonoptimal) spatial alignment with the QD [Fig. 6(c)]. The results, displayed in Fig. 8, show that this is indeed the case. In Fig. 8(a), for example, we see a symmetric spectrum, consistent with both modes being equally spatially coupled to the QD and equally (and oppositely) spectrally detuned from it. In Figs. 8(b) and 8(c), we see that the spectra are no longer symmetric, as the QD is on resonance with the high frequency mode in Fig. 8(b), and with the low frequency mode in Fig. 8(c). In each case we see Rabi splitting about the mode on resonance with the QD and only a small shift for the detuned mode. The Rabi splitting between the peaks is no longer at the maximum value of $2\sqrt{2}g_0$, but at a value closer to $2g_0$ due to the spatial misalignment of the QD with the empty-cavity standing wave modes.

Before moving on to study different parameter regimes for $\{g_0,\beta,\kappa,\gamma_\perp\}$, we examine the cavity's transmission spectrum as a function of the spectral detuning of the QD ($\Delta\omega_{ac}$). In practice [1–3], QD-cavity detuning is often achieved by varying the sample temperature, which tunes at different rates the transition frequency of the QD (due to its temperature-dependent energy bandgap) and the cavity mode (due to its temperature-dependent refractive index). More recently, gas condensation on the sample surface [49] has been successfully used to tune the cavity mode frequency of a surface-sensitive photonic crystal microcavity. Such a method has recently been shown to be effective for the microdisks studied here owing to the field localization at the top and bottom surface and at the disk periphery [50]. In Fig. 9 we plot the cavity transmission minima as a function of $\Delta\omega_{ac}$ for the parameter set studied above in Fig. 8, where the QD is spatially coupled to both standing wave modes of the microdisk. When the QD is far detuned from the standing wave cavity modes, we see the response of an essentially uncoupled system, with transmission dips at the bare QD and cavity mode frequencies ($\pm\beta$). In the center of the plot, as the QD is tuned through the bare-cavity resonances, a pair of

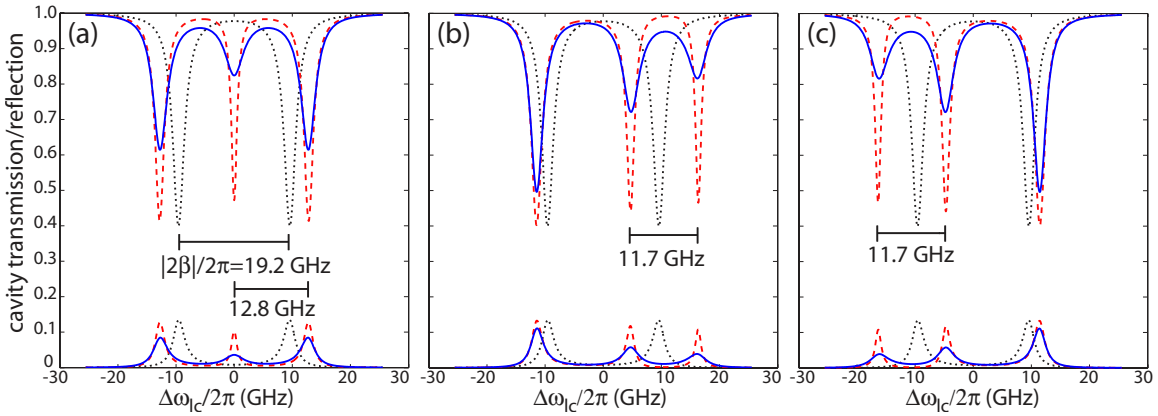

FIG. 8. (Color online) Steady state QME solution for the normalized optical transmission (top curves) and reflection (bottom curves) spectra of a QD coupled to a microdisk cavity under weak driving and for three different QD detunings: (a) $\Delta\omega_{ac}=0$, (b) $\Delta\omega_{ac}=\beta$, and (c) $\Delta\omega_{ac}=-\beta$. These plots are calculated for identical parameters as those in Fig. 5 with the exception that the phase of the backscattering parameter β has been changed from $\xi=0$ to $\xi=\pi/2$ ($\beta/2\pi=i9.6$ GHz).

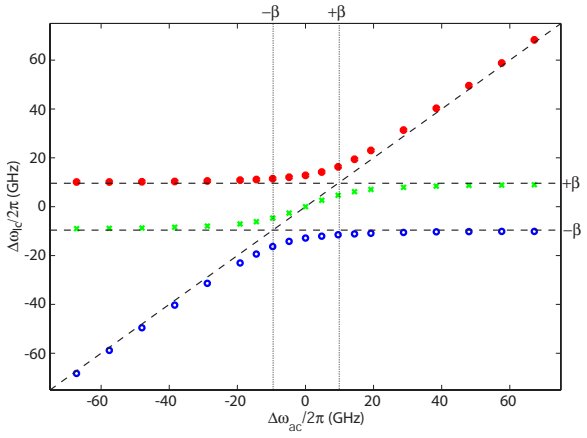

FIG. 9. (Color online) Position of the resonance dips within the transmission spectrum of a QD coupled to a microdisk cavity under weak driving, as a function of QD-cavity detuning $\Delta\omega_{ac}$. $\{g_0,\beta,\kappa_T,\kappa_e,\gamma_\parallel,\gamma_p\}/2\pi=\{6,i9.6,1.2,0.44,0.16,2.4\}$ GHz, so that the QD is spatially coupled to both standing wave cavity modes.

anti-crossings are evident as the QD couples to each of the standing wave modes of the microdisk.

B. $g_0>\beta>(\kappa_T,\gamma_\perp)$

Here we switch regimes to one in which the QD-cavity coupling rate dominates all other rates in the system, including the backscattering rate β. In particular, we choose $g_0/2\pi=12$ GHz, with $\beta/2\pi=4.8$ GHz, $\kappa_T/2\pi=1.2$ GHz ($\kappa_e/2\pi=0.44$ GHz), and $\tau_{sp}=1$ ns ($\gamma_\parallel/2\pi\sim0.16$ GHz). The qualitative behavior that we expect to see is similar to that of the previous section as both g_0 and β represent coherent processes, so that their relative values are not as important as their values in comparison to the dissipative rates in the system. This is seen in Fig. 10(a), where the QD is spectrally located at $-\beta$, so that it is resonant with the low frequency mode of the standing wave doublet. Predictably, the interaction with the QD causes this resonance to split, with a splitting $\Omega_R=2\sqrt{2}g_0$. The higher frequency mode remains unaffected, as the choice of $\xi=0$ causes it to be spatially misaligned with the QD.

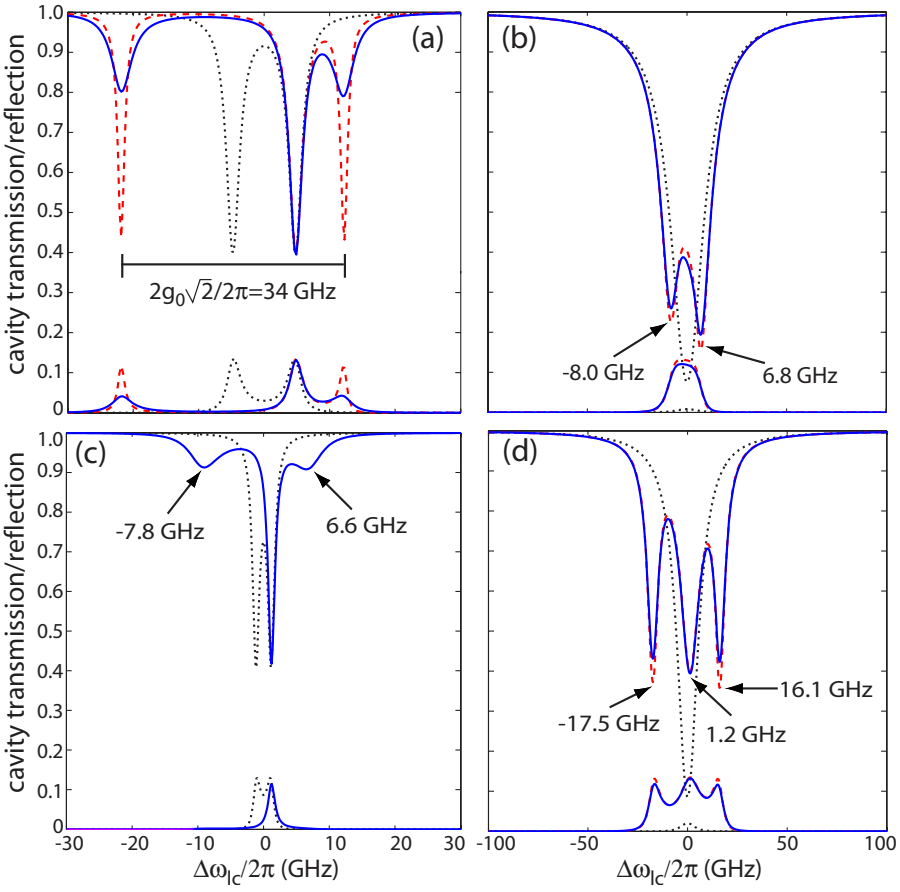

FIG. 10. (Color online) Steady state QME solution to the normalized optical transmission (top curves) and reflection (bottom curves) spectra of a QD coupled to a microdisk cavity with $\xi=0$, and for (a) $g_0>\beta>\kappa_T>\gamma_\perp$ ($\Delta\omega_{ac}=-\beta/2\pi$, $\{g_0,\beta,\kappa_T,\kappa_e,\gamma_\parallel,\gamma_p\}/2\pi=\{12,4.8,1.2,0.44,0.16,2.4\}$ GHz), (b) $\kappa_T>g_0>\beta>\gamma_\perp$ ($\Delta\omega_{ac}=0$, $\{g_0,\beta,\kappa_T,\kappa_e,\gamma_\parallel,\gamma_p\}/2\pi=\{6,1.2,9.6,3.5,0.16,0.7\}$ GHz), (c) $\gamma_\parallel>g_0>\beta>\kappa_T$ ($\Delta\omega_{ac}=-\beta/2\pi$, $\{g_0,\beta,\kappa_T,\kappa_e,\gamma_\parallel,\gamma_p\}/2\pi=\{6,1.2,0.6,0.22,9.4,0\}$ GHz), and (d) $g_0>\kappa_T>\beta>\gamma_\perp$ ($\Delta\omega_{ac}=0$, $\{g_0,\beta,\kappa_T,\kappa_e,\gamma_\parallel,\gamma_p\}/2\pi=\{12,1.2,6,2.2,0.16,0.7\}$ GHz). In these plots the additional black dotted line plots correspond to an empty cavity ($g_0=0$) and the red dashed line plots correspond to a QD with no nonradiative dephasing ($\gamma_p/2\pi=0$ GHz).

C. $\kappa_T > g_0 > \beta > \gamma_\perp$

Now, we take the cavity loss rate $\kappa_T/2\pi=9.6$ GHz to exceed both $g_0/2\pi=6$ GHz and $\beta/2\pi=1.2$ GHz. In addition, $\kappa_e/2\pi=3.5$ GHz, $\gamma_\parallel/2\pi=0.16$ GHz, and $\gamma_p/2\pi=0$ or 0.7 GHz, so that $\kappa_T > \kappa_e > \gamma_\perp$ (good cavity limit). In the absence of a QD we expect to see a single transmission dip rather than a doublet for $\kappa_T \gg \beta$. This is confirmed in simulation by the black dotted line in Fig. 10(b). With the addition of a QD, taken to be resonant with the center frequency of the single cavity transmission dip, we expect to see this single dip split into two, with the dips not being completely resolved due to decay of the cavity mode ($\kappa_T > g$). This is confirmed in Fig. 10(b), where the splitting $\Omega_R/2\pi=14.8$ GHz lies between the expected splitting for a purely traveling wave cavity mode ($\Omega_R=2g_0$) and the expected splitting for a purely standing wave cavity mode ($\Omega_R=2\sqrt{2}g_0$), and lies closer to the former due to the large degree to which κ_T exceeds β.

D. $\gamma_\parallel > g_0 > \beta > \kappa_T$

Here, the roles of κ_T and $\gamma_\parallel$ are swapped in comparison to the previous subsection, so that $\gamma_\parallel/2\pi=9.6$ GHz is the dominant dissipative rate, exceeding each of $\{g_0, \beta, \kappa_T, \kappa_e\}/2\pi = \{6, 1.2, 0.6, 0.22\}$ GHz (bad cavity limit). Unlike our previous example, in absence of a QD we do expect to see a pair of standing wave modes form, as $\beta > \kappa_T$. This is confirmed in Fig. 10(c) (black dashed line). Now, we introduce a QD that is spectrally aligned with the low frequency mode at $-\beta$. Because QD decay is so large in this case we expect that the standing wave character of the modes is going to largely be erased when coupled to the QD. To confirm this intuition, we examine the calculated transmission spectrum in Fig. 10(c). The low frequency mode does indeed split, but the splitting $\Omega_R/2\pi=14.4$ GHz is less than the expected splitting of $2\sqrt{2}g_0$ for standing wave modes, and lies much closer to the $2g_0$ splitting for traveling wave modes. The situation thus mimics that of the previous example, although in this case the relatively weak transmission contrast of the QD-coupled resonances is a result of operation in the bad cavity limit.

E. $g_0 > \kappa_T > \beta > \gamma_\perp$

Finally, we consider a scenario in which the QD-cavity coupling $g_0/2\pi=12$ GHz is the dominant rate in the system, but where cavity decay $\kappa_T/2\pi=6$ GHz exceeds the backscattering rate $\beta/2\pi=1.2$ GHz. In absence of a QD we see a single transmission resonance dip [Fig. 10(d)] as $\kappa_T > \beta$. If a QD is now spectrally aligned to the center of this transmission dip ($\Delta\omega_{ac}=0$) three resonances appear within the transmission spectrum of Fig. 10(d). This should be contrasted with the transmission spectrum of Fig. 10(b) in which only two resonant transmission dips were present. The central resonance dip of Fig. 10(d) is at a detuned frequency of 1.2 GHz ($=\beta/2\pi$), and corresponds to the frequency of one of the two standing wave modes that can form through an appropriate combination of the traveling wave modes. As this mode is spatially misaligned from the QD for $\xi=0$, we do not expect its frequency to have shifted due to interaction with the QD. The other two transmission resonances correspond to the splitting of the low frequency mode from its empty-cavity position at $-\beta/2\pi=-1.2$ GHz. The splitting of $\Omega_R/2\pi=33.6$ GHz is very close to the value of $2\sqrt{2}g_0$ expected for interaction with a standing wave mode.

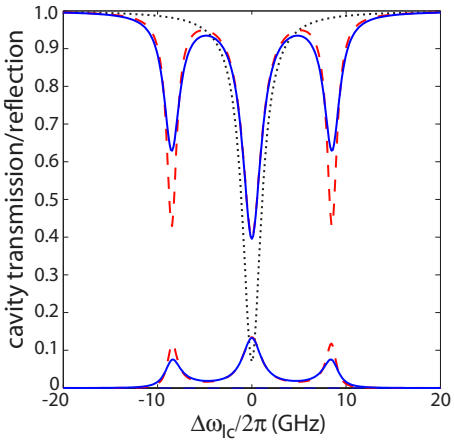

FIG. 11. (Color online) Steady state QME solution for the normalized optical transmission (top curves) and reflection (bottom curves) spectra for a QD coupled to a microdisk cavity under weak driving and with the roughness-induced backscattering rate (β) zero. $g_0 > \kappa_T > \gamma_\perp > \beta$ ($\Delta\omega_{ac}=0$, $\{g_0, \beta, \kappa_T, \kappa_e, \gamma_\parallel, \gamma_p\}/2\pi = \{6, 0, 1.2, 0.44, 0.16, 0.7\}$ GHz). The additional black dotted line plots correspond to an empty cavity ($g_0=0$) and the red dashed lines plots correspond to a QD with no nonradiative dephasing ($\gamma_p/2\pi=0$ GHz).

The basic result that the above example demonstrates is that the QD can effectively serve as a means to couple the traveling wave microdisk modes, even in instances where the backscatter parameter is small relative to other rates in the system. As a final illustration of this, we consider the situation where the backscatter parameter is zero. In Fig. 11, the empty-cavity single transmission resonance separates into three resonance dips, one at the original zero detuning and the other two split by $2\sqrt{2}g_0$. The interpretation of this result is that the QD has effectively served to couple the two counter-propagating traveling wave modes, creating a pair of standing wave resonant modes, one which is decoupled and has an electric field node at the position of the QD, and the other which is strongly coupled to the QD at a field antinode. In this case, and in other strong coupling cases where g_0 is the dominant system rate, the QD serves to set the position of the effective standing wave cavity modes (as opposed to backscattering phase ξ) thus ensuring azimuthal alignment of the QD with a field antinode of one of the standing wave modes. Note that in the example of IV A (Fig. 5) in which $\beta > g_0$, it is the phase of β (ξ) which determines the position of the standing wave field antinodes with respect to the QD.

V. INTENSITY CORRELATION FUNCTION CALCULATIONS

Of additional interest is the behavior of the (normalized) intensity correlation function $g^{(2)}(\tau)$, whose value can indicate nonclassical characteristics of the cavity field [51], and

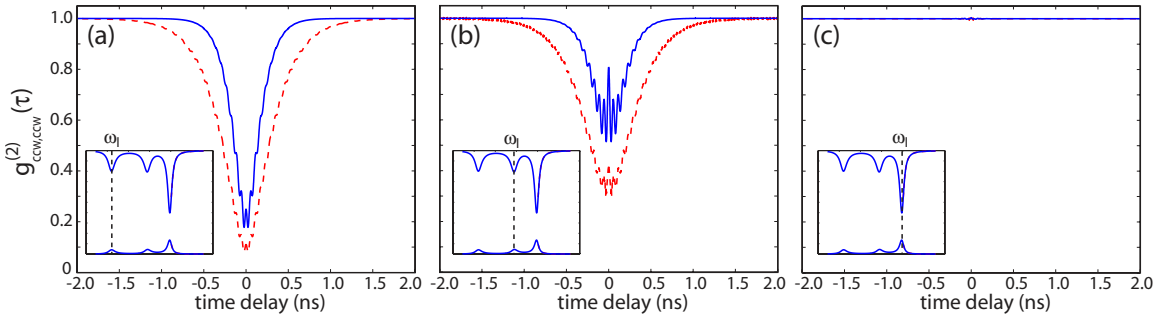

FIG. 12. (Color online) Normalized second order autocorrelation function (solid blue line) $g^{(2)}_{\mathrm{CCW,CCW}}(\tau)$ for the counterclockwise propagating cavity mode for the parameters $\{g_0,\beta,\kappa_T,\kappa_e,\gamma_\parallel,\gamma_p\}/2\pi=\{6,9.6,1.2,0.44,0.16,2.4\}$ GHz, $\Delta\omega_{ac}=-\beta$, and whose transmission/reflection spectrum, originally shown in Fig. 5(c), is redisplayed here in the plot insets. (a) $\omega_l=-\beta-g_0\sqrt{2}$, (b) $\omega_l=-\beta+g_0\sqrt{2}$, and (c) $\omega_l=\beta$. The additional red dashed line plots correspond to a QD with no nonradiative dephasing ($\gamma_p/2\pi=0$ GHz).

is thus of essential importance in the characterization of QD-cavity based devices such as single photon sources [12,52–54]. Furthermore, intensity correlations of the cavity field (and other higher-order correlations) are sensitive to the energy levels of multi-photon states of the system, and thus provide further information about the system beyond the weak driving limit studied above. This is particularly important in the case of WGM cavities, in which the presence of a double-peaked spectrum typically associated with Rabi splitting cannot by itself be regarded as evidence for strong coupling. Here we analyze the intensity correlations of a coupled QD-cavity system, the cavity containing a pair of nearly degenerate WGM modes as in the analysis of the previous sections.

A general definition for any (stationary) two-time intensity correlation function in our system is [55,56]

$$g^{(2)}_{a,b}(\tau)=\lim_{t\to\infty}\frac{\langle\hat{a}^\dagger(t)\hat{b}^\dagger(t+\tau)\hat{b}(t+\tau)\hat{a}(t)\rangle}{\langle\hat{a}^\dagger(t)\hat{a}(t)\rangle\langle\hat{b}^\dagger(t+\tau)\hat{b}(t+\tau)\rangle},\qquad(23)$$

where $\hat{a}$ and $\hat{b}$ are the field annihilation operators for modes a and b, which can be the cavity traveling wave modes (labeled CW/CCW) or standing wave modes (labeled $\mathrm{SW}_1/\mathrm{SW}_2$). Here, it is assumed that steady-state has been reached (i.e., $t\to\infty$), so $g^{(2)}_{a,b}(\tau)$ is the stationary two-time correlation function, and is a function of the time delay τ only. We calculate $g^{(2)}_{a,b}(\tau)$ by applying the quantum regression theorem [37] and numerically integrating the quantum master equation [Eqs. (11)–(16)] [42,43]. In what follows, we initially focus on calculating $g^{(2)}_{\mathrm{CCW,CCW}}(\tau)$, the two-time intensity auto-correlation function for the counterclockwise WGM field operator $\hat{a}_{\mathrm{CCW}}$. Due to phasematching, the reflected signal from the cavity is proportional to $\hat{a}_{\mathrm{CCW}}$, allowing such intensity correlations to be measured in practice.

We begin by considering the set of parameters studied in the steady-state transmission and reflection spectrum of Fig. 5(c), where $\xi=0$ so that β is purely real and positive, and where $\Delta\omega_{ac}=-\beta$ so that the QD is tuned to resonance with the empty cavity lower frequency standing wave mode which it is spatially aligned with. $g^{(2)}_{\mathrm{CCW,CCW}}(\tau)$ is calculated in three instances, with each case corresponding to a probe field frequency ω_l tuned onto resonance with one of the three resonance peaks in the coupled cavity-QD reflection spectrum of Fig. 5(c). The results are shown in Fig. 12. For probe frequencies $\omega_l=-\beta\pm g_0\sqrt{2}$ [Figs. 12(a) and 12(b)], photon antibunching and sub-Poissonian statistics are predicted. This antibunching is a result of the anharmonicity of the Jaynes-Cummings system; once the system absorbs a photon at $-\beta\pm g_0\sqrt{2}$, absorption of a second photon at the same frequency is not resonant with the higher excited state of the system [12]. The degree of antibunching is a function of the specific system parameters chosen, and $g^{(2)}_{\mathrm{CCW,CCW}}(0)$ approaches zero more closely as g_0 further exceeds the rates κ_T and $\gamma_\perp$. In this case, the difference in $g^{(2)}_{\mathrm{CCW,CCW}}(\tau)$ for probe frequencies $\omega_l=-\beta\pm g_0\sqrt{2}$ is a result of the asymmetry in the spectrum of the system due to the presence of the nominally uncoupled high-frequency standing wave mode [asymmetry in the probe frequency detuning from the CCW traveling wave mode's natural frequency also plays a role here, and has a persistent effect upon $g^{(2)}_{\mathrm{CCW,CCW}}(\tau)$ even for increasing mode-coupling (β,g_0) and decreasing dephasing $(\kappa_T,\gamma_\perp)$]. For a probe frequency resonant with the third reflection peak at $\omega_l=\beta$ [Fig. 12(c)], $g^{(2)}_{\mathrm{CCW,CCW}}(\tau)$ is essentially unity for all times and the reflected light from the cavity is nearly Poissonian due to the spatial misalignment, and resulting decoupling, of the QD from the high-frequency cavity mode light field.

We next examine the parameter set explored in Fig. 8(a), where $\xi=\pi/2$, so that both standing wave cavity modes are spatially coupled to the QD. In addition, $\Delta\omega_{ac}=0$, so that the modes are equally and oppositely detuned from the QD. Once again, we calculate $g^{(2)}_{\mathrm{CCW,CCW}}(\tau)$ for three cases, with each case corresponding to ω_l on resonance with one of the three peaks in the reflection spectrum of Fig. 8(a). The results, shown in Fig. 13, indicate mild antibunching for $\omega_l/2\pi=\pm 12.8$ GHz (the leftmost and rightmost peaks in the reflection spectrum) and for $\gamma_p=0$. Higher levels of nonradiative dephasing lead to a washing out of the antibunching, though the field exhibits sub-Poissonian statistics on a time scale of $\sim 1/(\kappa_T+\gamma_\perp)/2$. For $\omega_l=0$ [Fig. 13(b)], the calculation predicts photon bunching. This occurs because the resonance at zero detuning only appears when at least one photon is in the cavity and is coupled to the QD, which then allows for an additional photon at this frequency to be stored in the cavity and reflected. The high-frequency oscillations in

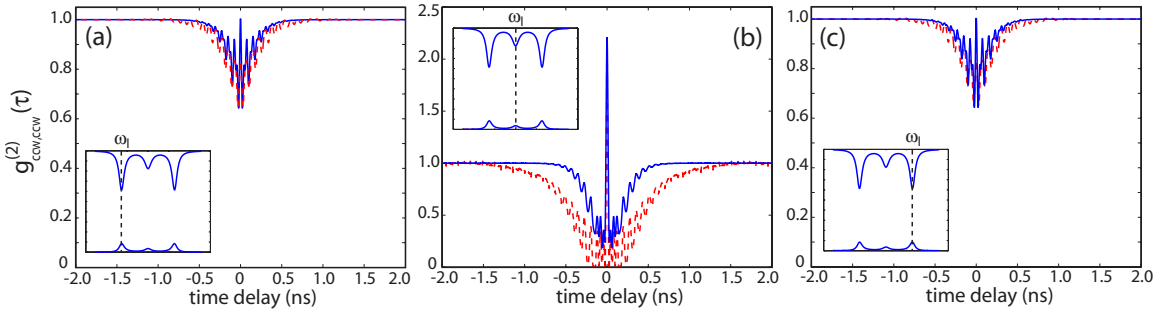

FIG. 13. (Color online) Normalized second order autocorrelation function (solid blue line) $g^{(2)}_{\mathrm{CCW,CCW}}(\tau)$ for the counterclockwise propagating cavity mode for the parameters $\{g_0,\beta,\kappa_T,\kappa_e,\gamma_\parallel,\gamma_p\}/2\pi=\{6,i9.6,1.2,0.44,0.16,2.4\}$ GHz, $\Delta\omega_{ac}=0$, and whose transmission/reflection spectrum, originally shown in Fig. 8(a), is redisplayed here in the plot insets. (a) $\omega_l/2\pi=-12.8$ GHz, (b) $\omega_l/2\pi=0$ GHz, and (c) $\omega_l/2\pi=12.8$ GHz. The additional red dashed line plots correspond to a QD with no nonradiative dephasing ($\gamma_p/2\pi=0$ GHz).

$g^{(2)}_{\mathrm{CCW,CCW}}(\tau)$, and resulting narrow super-Poissonian central peak about $g^{(2)}_{\mathrm{CCW,CCW}}(0)$, are a result of interference effects created by beating between the two cavity modes that are excited in this case (note that the central resonance peak in the cavity-QD spectrum is predominantly atomic-like, and excitation through the optical channel effectively excites the two detuned peaks, which are primarily photonic in nature).

Finally, we consider the parameter set explored in Fig. 11, where $\beta=0$ so that only the QD couples the clockwise and counterclockwise modes together. For the Rabi-split peaks centered at $\omega_l=\pm g_0\sqrt{2}$, we see strong antibunching, as to be expected for a single QD coupled to a single cavity mode excited on resonance with the Rabi-split peaks. At $\omega_l=0$, there are just minor oscillations about $g^{(2)}(\tau)=1$ due to the weak and transient coupling of the resonant cavity mode with the QD. Comparison of this example with that of Fig. 13 illustrates well the added system information gained by studying intensity correlations of the scattered light. Although both systems look very similar when studying the amplitude of light transmission and reflection intensity under weak driving, the intensity correlations provide information about the spatial position of the QD relative to each of the standing wave cavity modes and the relative strength of g_0 to β.

Up to this point we have considered only the two-time correlation function for the counterclockwise propagating cavity mode. Correlation functions for the clockwise propagating mode and standing wave cavity modes can be determined through formulas analogous to Eq. (23), and can provide further insight into the appropriateness of the standing wave mode picture. Figure 15 shows the results of two-time intensity correlation calculations for the set of parameters considered in Fig. 14, where now we have plotted the intensity autocorrelation function for the standing wave modes. The results are consistent with the standing wave mode picture of atom-cavity interaction: mode SW_1 is spatially aligned with the QD, and hence $g^{(2)}_{\mathrm{SW}_1,\mathrm{SW}_1}(\tau)$ shows significant photon antibunching at the Rabi-split frequencies $\omega_l=\pm g_0\sqrt{2}$ and off-resonance bunching [12] at $\omega_l=0$ [top plots in Figs. 15(a)–15(c)], while standing wave mode SW_2 is spatially misaligned from the QD and $g^{(2)}_{\mathrm{SW}_2,\mathrm{SW}_2}(\tau)$ is essentially unity for all drive frequencies [bottom plots in Figs. 15(a)–15(c)].

In addition to the autocorrelation calculations presented thus far, there are a number of other investigations of nonclassical behavior within this system that may be of interest. For example, mixed-mode correlation functions can give insight into entanglement between the two cavity modes and the potential for generating non-classical states such as those employed in studies of the Einstein-Podolsky-Rosen paradox [55,57]. Squeezing, which has been studied in the context of the Jaynes-Cummings system by a number of authors [39,58–61], is also a potential topic for further study. The strong coupling of two cavity modes to a single QD, in the

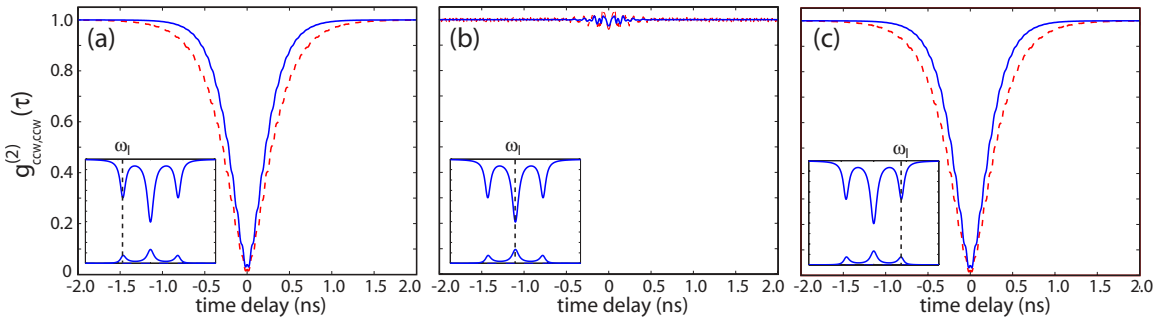

FIG. 14. (Color online) Normalized second order correlation function (solid blue line) $g^{(2)}_{\mathrm{CCW,CCW}}(\tau)$ for the counterclockwise propagating cavity mode for the parameters $\{g_0,\beta,\kappa_T,\kappa_e,\gamma_\parallel,\gamma_p\}/2\pi=\{6,0,1.2,0.44,0.16,0.7\}$ GHz, $\Delta\omega_{ac}=0$, and whose transmission/reflection spectrum, originally shown in Fig. 11, is redisplayed here in the plot insets. (a) $\omega_l=-g_0\sqrt{2}$, (b) $\omega_l=0$, and (c) $\omega_l=g_0\sqrt{2}$. The additional red dashed line plots correspond to a QD with no nonradiative dephasing ($\gamma_p/2\pi=0$ GHz).

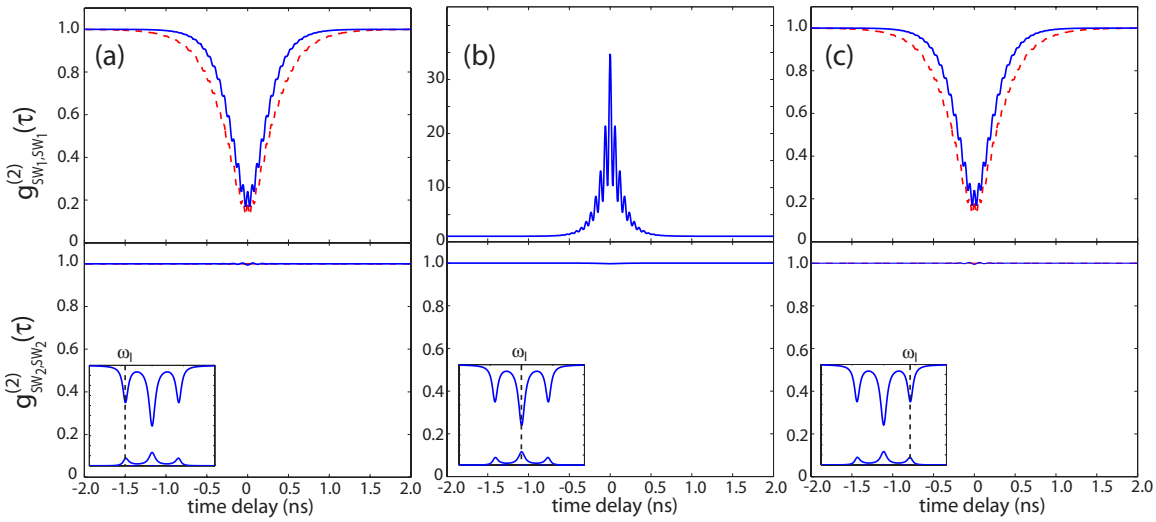

FIG. 15. (Color online) Normalized second order correlation functions (solid blue line) $g^{(2)}_{SW_1,SW_1}(\tau)$ (top plots) and $g^{(2)}_{SW_2,SW_2}(\tau)$ (bottom plots) for the parameters $\{g_0,\beta,\kappa_T,\kappa_e,\gamma_\parallel,\gamma_p\}/2\pi=\{6,0,1.2,0.44,0.16,0.7\}$ GHz, $\Delta\omega_{ac}=0$, and whose transmission/reflection spectrum, originally shown in Fig. 11, is redisplayed here in the plot insets. (a) $\omega_l=-g_0\sqrt{2}$, (b) $\omega_l=0$, and (c) $\omega_l=g_0\sqrt{2}$. The additional red dashed line plots correspond to a QD with no non-radiative dephasing ($\gamma_p/2\pi=0$ GHz).

presence of background-mediated intermodal coupling, may yield important differences from previously studied systems. Furthermore, generating squeezed light or other nonclassical fields in a microchip-based geometry could be of technological importance. In the Appendix, we present some preliminary calculations on the above topics which indicate the degree to which such nonclassical behavior may be exhibited in these devices. A more authoritative treatment of these topics requires a systematic investigation of different parameter regimes for $\{g_0,\beta,\kappa_T,\kappa_e,\gamma_\parallel,\gamma_p\}$, driving field strength and frequency, and excitation channel (coupling to the cavity mode versus coupling to the QD directly), and is beyond the scope of this paper.

VI. SUMMARY

We have extended the standard quantum master equation model for a two-level system coupled to the mode of an electromagnetic cavity to better reflect the situation that occurs in realistic semiconductor microdisk cavities. In this model the quantum dot, still treated as a two-level system, is coupled to two cavity modes corresponding to clockwise and counterclockwise propagating whispering-gallery modes of the disk. These two modes are in turn passively coupled to each other through surface roughness, characterized by a backscatter parameter β. We examine the steady state behavior of the system for differing regimes of β, the QD-cavity coupling rate g_0, the cavity decay rate κ_T, and the quantum dot dephasing rate $\gamma_\perp$. In particular, we consider conditions for which standing wave cavity modes form, how the magnitude of the different system rates and the phase of β determine the nodes and antinodes of the cavity modes with respect to the quantum dot, and the resulting QD-cavity coupling. It is anticipated that this analysis will be useful in the interpretation of experimental spectra from a waveguide-coupled whispering-gallery-mode microcavity strongly coupled to a single two-level system such as the exciton state of a self-assembled quantum dot.

ACKNOWLEDGMENTS

K.S. acknowledges the Hertz Foundation and K.S. and O.P. acknowledge the Caltech Center for the Physics of Information for support of this work.

APPENDIX: NONCLASSICAL CORRELATIONS AND SQUEEZING

1. Mixed-mode correlation function

We reconsider the parameter set of Fig. 14, where $\beta=0$, so that only the QD is coupling the two cavity modes, and calculate the mixed-mode correlation functions $g^{(2)}_{CW,CCW}(\tau)$ and $g^{(2)}_{SW_1,SW_2}(\tau)$ for the same set of parameters. We focus on solutions for $\tau=0$, which can be obtained entirely from the steady-state density matrix, and examine the behavior of $g^{(2)}_{a,b}(0)$ as a function of driving frequency. The Cauchy-Schwarz inequality

$$(g^{(2)}_{a,b})^2 \leqslant g^{(2)}_{a,a} * g^{(2)}_{b,b} \tag{A1}$$

is violated when nonclassical correlations exist between the two modes a and b [55,56]. As we see in Fig. 16(a), this inequality is violated for the traveling wave modes at particular choices of ω_l, so that nonclassical correlations between the two modes can occur in this system. On the other hand, for the standing wave modes, no quantum correlations exist, as mode SW_2 is not coupled to the QD, so that $g^{(2)}_{SW_1,SW_2}(0)=g^{(2)}_{SW_2,SW_2}(0)=1$ for all ω_l. The transient (i.e., nonsteady-state) behavior of the mixed and single mode correlation functions are shown in Fig. 16(b). Here we plot $g^{(2)}_{CW,CCW}(t)$, $g^{(2)}_{SW_1,SW_2}(t)$, $g^{(2)}_{CW,CW}(t)$, $g^{(2)}_{CCW,CCW}(t)$, $g^{(2)}_{SW_1,SW_1}(t)$, and $g^{(2)}_{SW_2,SW_2}(t)$ for $\omega_l/2\pi=-6$ GHz (where the Cauchy-

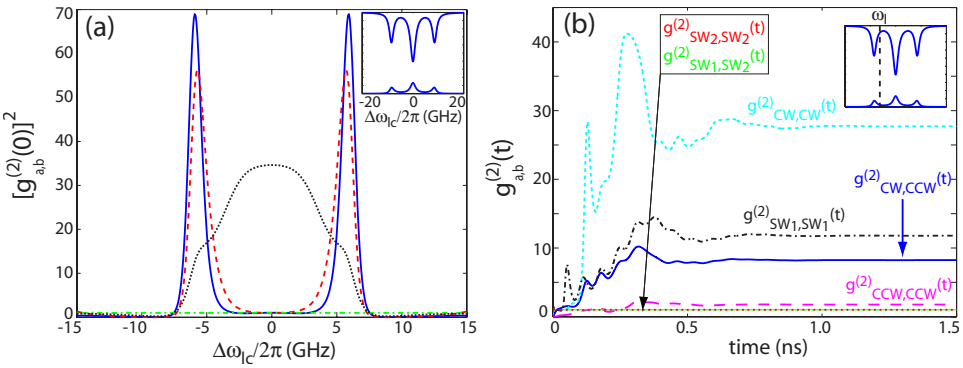

FIG. 16. (Color online) Second order correlation functions for the parameters $\{g_0,\beta,\kappa_T,\kappa_e,\gamma_\parallel,\gamma_p\}/2\pi=\{6,0,1.2,0.44,0.16,0.7\}$ GHz, $\Delta\omega_{ac}=0$, and whose transmission/reflection spectrum, originally shown in Fig. 11, is redisplayed here in the plot insets. (a) $[g^{(2)}_{CW,CCW}(0)]^2$ (solid blue line), $g^{(2)}_{CW,CW}(0)*g^{(2)}_{CCW,CCW}(0)$ (dashed red line), $[g^{(2)}_{SW_1,SW_2}(0)]^2$ (dash-dotted green line), and $g^{(2)}_{SW_1,SW_1}(0)*g^{(2)}_{SW_2,SW_2}(0)$ (dotted black line) as a function of laser-cavity detuning. (b) $g^{(2)}_{CW,CCW}(t)$, $g^{(2)}_{CW,CW}(t)$, $g^{(2)}_{CCW,CCW}(t)$, $g^{(2)}_{SW_1,SW_2}(t)$, $g^{(2)}_{SW_1,SW_1}(t)$, and $g^{(2)}_{SW_2,SW_2}(t)$ for excitation at $\omega_l/2\pi=-6$ GHz, and when both cavity modes are initially in the vacuum state and the QD is in its ground state.

Schwarz inequality is nearly maximally violated), with the $t=0$ initial state consisting of both cavity modes in the vacuum state and the QD in its ground state. The calculations indicate that steady-state behavior is achieved after ~1 ns, corresponding to the system's average decay time $(\sim 1/(\kappa_T+\gamma_\perp)/2)$, with violations of the Cauchy-Schwarz inequality for the traveling wave modes occurring after only ~0.2 ns.

2. Squeezing

As has been observed by several other authors in studies of single mode CQED [58,60], squeezing in the field quadratures can occur, however, with the amount of squeezing typically small (<20%) unless large intracavity photon numbers (>10) are achieved.[1] The basic reason for this is that the nonlinear interaction that generates squeezing in the Jaynes-Cummings system is that of the electromagnetic field coupling to a saturable oscillator (the QD); this implies that the intracavity field has to be strong enough for QD saturation effects to be appreciable. For our system, situations where only one of the standing wave modes is coupled to the QD (as in Figs. 12 and 14, for example) essentially reduce to that of the single mode cavity QED case, and we expect qualitatively similar behavior. A perhaps more interesting example to study is that of Fig. 13, where both standing wave modes are equally coupled to a QD. To achieve a reasonable intracavity photon number, we increase the input driving field by approximately three orders of magnitude over the weak drive fields we have used up to this point, to a level of ~30 photons/ns, so that the average intracavity photon number [bottom of Fig. 17(b)] peaks at a value of ~1. This results in the transmission and reflection spectra shown at the top of Fig. 17(a). In comparison to the transmission/reflection spectra calculated in the weak driving limit in Fig. 8(a), we now begin to see asymmetries in the transmission dips (reflection peaks) that are associated with multiphoton transitions to excited states in the Jaynes-Cummings spectrum and QD saturation effects. In this calculation, we are unable to numerically study higher drive strengths due to the resulting large system size for these two-mode cavities. To access higher driving fields using the same computational resources, adopting a wavefunction-based approach (i.e., the quantum Monte Carlo method) is one possibility.

We next consider fluctuations in the steady-state, internal cavity field (squeezing in the external field, which can be investigated through the spectrum of squeezing [62], for example, are not considered here but may be of future interest). First, we look at fluctuations in the photon number in mode i by calculating the Mandel Q parameter [51]

$$Q(\hat{n}_i)=\frac{\mathrm{Var}(\hat{a}_i^\dagger\hat{a}_i)-\langle\hat{a}_i^\dagger\hat{a}_i\rangle}{\langle\hat{a}_i^\dagger\hat{a}_i\rangle}, \tag{A2}$$

where for some operator $\hat{O}$, $\mathrm{Var}(\hat{O})=\langle\hat{O}^2\rangle-\langle\hat{O}\rangle^2$. Figure 17(c) shows the calculated Q parameter as a function of driving field frequency for the CW/CCW traveling wave modes (top) and SW_1/SW_2 standing wave modes (bottom). These plots show $Q<0$ for certain driving frequencies, indicating that sub-Poissonian photon number statistics can be achieved, though the level of nonclassicality is small (~5%). A calculation of $Q(\hat{n}_{CW})(t)$ for $\omega_l=0$ (with both cavity modes initially in the vacuum state and the QD in its ground state) indicates that slightly higher levels of nonclassicality ($Q\sim-0.1$) can be achieved before steady-state is reached. Additional preliminary calculations using a quantum Monte Carlo method to access higher drive strengths have been performed, and show that Q can continue to de-

[1]It should be noted that Refs. [58,60] study the Jaynes-Cummings system in absence of a driving field. Strong driving fields significantly affect the structure of the Jaynes-Cummings systems, causing drive-strength-dependent Stark shifts of the system eigenergies [63]. We thus might expect strong driving fields to have an appreciable affect on squeezing and photon statistics. In particulars, Alsing and co-workers [63] have shown that squeezed, displaced number states are eigenstates of the total Hamiltonian for the driven Jaynes-Cummings model.

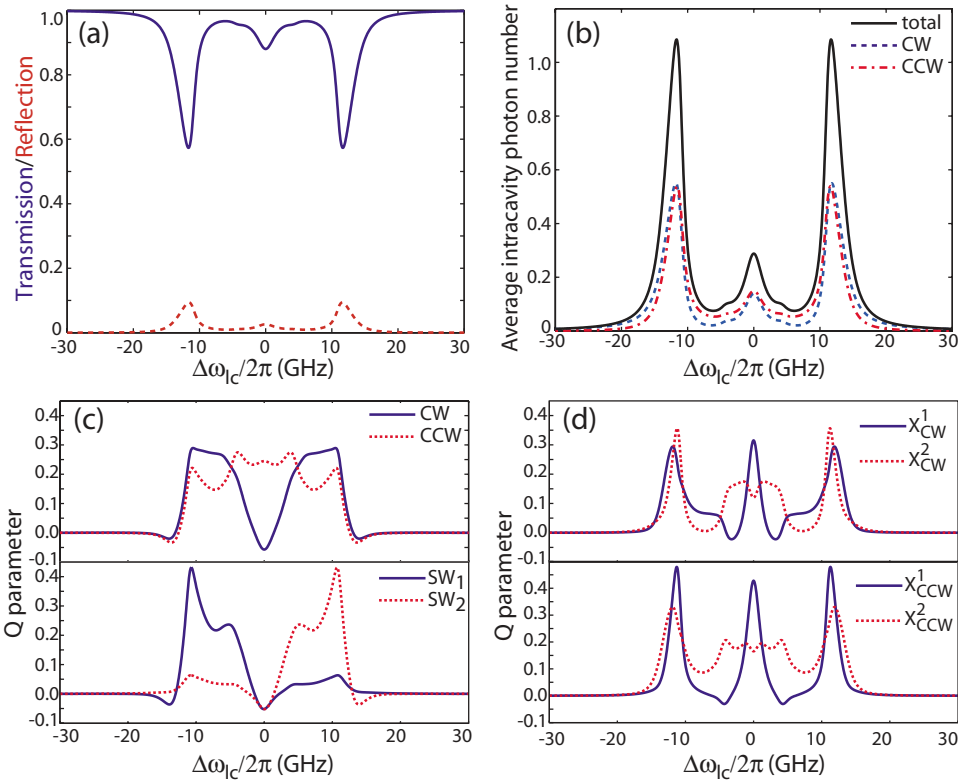

FIG. 17. (Color online) Nonclassical properties of the microdisk cavity-QD system under more intense driving (~30 photons/ns drive power), and with system parameters $\{g_0, \beta, \kappa_T, \kappa_e, \gamma_\parallel, \gamma_p\}/2\pi = \{6, i9.6, 1.2, 0.44, 0.16, 0.7\}$ GHz. (a) Cavity transmisson/reflection as a function of driving field frequency ω_l, (b) total (solid black line), CW mode (dashed blue line), and CCW mode (dot-dashed red line) intracavity photon number as a function of ω_l, (c) Q parameter for the intracavity photon number in the (top) traveling wave WGMs and (bottom) standing wave WGMs. (d) Q parameter for the X^1 and X^2 quadratures of the (top) CW and (bottom) CCW traveling wave mode.

crease for larger driving fields. For drive strengths of ~300 photons/ns (corresponding to an average total intracavity photon number ~1 at $\omega_l = 0$), $Q(\hat{n}_{\mathrm{CW}})$ can reach −0.35 in its transient (non-steady-state) behavior.

Similarly, one can examine fluctuations in the field quadratures. For mode i, we define the quadrature operators $\hat{X}_i^{1,2}$ by

$$\hat{X}_i^1 = \frac{1}{2}(\hat{a}_i + \hat{a}_i^\dagger),$$

$$\hat{X}_i^2 = \frac{-i}{2}(\hat{a}_i - \hat{a}_i^\dagger). \tag{A3}$$

The corresponding Q parameter for quadrature j of mode i is then [56]

$$Q_i^j = \frac{\mathrm{Var}(\hat{X}_i^j) - 0.25}{0.25}. \tag{A4}$$

From Fig. 17(d), we see that small amounts of quadrature squeezing in the CW/CW modes are apparent for the conditions considered.

[1] J. P. Reithmaier, G. Sek, A. Loffer, C. Hoffman, S. Kuhn, S. Reitzenstein, L. V. Keldysh, V. D. Kulakovskii, T. L. Reinecke, and A. Forchel, Nature (London) **432**, 197 (2004).
[2] T. Yoshie, A. Scherer, J. Hendrickson, G. Khitrova, H. Gibbs, G. Rupper, C. Ell, Q. Schenkin, and D. Deppe, Nature (London) **432**, 200 (2004).
[3] E. Peter, P. Senellart, D. Martrou, A. LemaÎtre, J. Hours, J. M. Gérard, and J. Bloch, Phys. Rev. Lett. **95**, 067401 (2005).
[4] H. J. Kimble, Phys. Scr. **T76**, 127 (1998).
[5] J. J. Sanchez-Mondragon, N. B. Narozhny, and J. H. Eberly, Phys. Rev. Lett. **51**, 550 (1983).
[6] G. S. Agarwal, Phys. Rev. Lett. **53**, 1732 (1984).
[7] Q. A. Turchette, C. J. Hood, W. Lange, H. Mabuchi, and H. J. Kimble, Phys. Rev. Lett. **75**, 4710 (1995).
[8] P. R. Rice and H. J. Carmichael, IEEE J. Quantum Electron. **24**, 1351 (1988).
[9] C. M. Savage and H. J. Carmichael, IEEE J. Quantum Electron. **24**, 1495 (1988).
[10] P. Alsing and H. J. Carmichael, Quantum Opt. **3**, 13 (1991).
[11] M. A. Armen and H. Mabuchi, Phys. Rev. A **73**, 063801

(2006).
[12] K. M. Birnbaum, A. Boca, R. Miller, A. Boozer, T. E. Northup, and H. J. Kimble, Nature (London) **436**, 87 (2005).
[13] L.-M. Duan and H. J. Kimble, Phys. Rev. Lett. **92**, 127902 (2004).
[14] R. J. Thompson, G. Rempe, and H. J. Kimble, Phys. Rev. Lett. **68**, 1132 (1992).
[15] C. J. Hood, T. W. Lynn, A. C. Doherty, A. S. Parkins, and H. J. Kimble, Science **287**, 1447 (2000).
[16] P. W. H. Pinske, T. Fischer, P. Maunz, and G. Rempe, Nature (London) **404**, 365 (2000).
[17] A. Boca, R. Miller, K. M. Birnbaum, A. D. Boozer, J. McKeever, and H. J. Kimble, Phys. Rev. Lett. **93**, 233603 (2004).
[18] J. C. Knight, G. Cheung, F. Jacques, and T. A. Birks, Opt. Lett. **22**, 1129 (1997).
[19] M. Cai, O. Painter, and K. J. Vahala, Phys. Rev. Lett. **85**, 74 (2000).
[20] D. K. Armani, T. J. Kippenberg, S. M. Spillane, and K. J. Vahala, Nature (London) **421**, 925 (2003).
[21] T. A. Birks and Y. W. Li, J. Lightwave Technol. **10**, 432 (1992).
[22] K. Srinivasan, P. E. Barclay, M. Borselli, and O. Painter, Phys. Rev. B **70**, 081306(R) (2004).
[23] P. E. Barclay, K. Srinivasan, and O. Painter, Opt. Express **13**, 801 (2005).
[24] M. Borselli, K. Srinivasan, P. E. Barclay, and O. Painter, Appl. Phys. Lett. **85**, 3693 (2004).
[25] K. Srinivasan, M. Borselli, T. J. Johnson, P. E. Barclay, O. Painter, A. Stintz, and S. Krishna, Appl. Phys. Lett. **86**, 151106 (2005).
[26] K. Srinivasan, M. Borselli, O. Painter, A. Stintz, and S. Krishna, Opt. Express **14**, 1094 (2006).
[27] D. S. Weiss, V. Sandoghdar, J. Hare, V. Lefèvre-Seguin, J.-M. Raimond, and S. Haroche, Opt. Lett. **20**, 1835 (1995).
[28] B. E. Little and S. T. Chu, Opt. Lett. **21**, 1390 (1996).
[29] T. J. Kippenberg, S. M. Spillane, and K. J. Vahala, Opt. Lett. **27**, 1669 (2002).
[30] M. Borselli, T. J. Johnson, and O. Painter, Opt. Express **13**, 1515 (2005).
[31] M. Rosenblit, P. Horak, S. Helsby, and R. Folman, Phys. Rev. A **70**, 053808 (2004).
[32] T. Aoki, B. Dayan, E. Wilcut, W. P. Bowen, A. S. Parkins, H. J. Kimble, T. J. Kippenberg, and K. J. Vahala, Nature (London) **443**, 671 (2006).
[33] K. Srinivasan, Ph.D. thesis, California Institute of Technology (Pasadena, 2006).
[34] M. L. Gorodetsky, A. D. Pryamikov, and V. S. Ilchenko, J. Opt. Soc. Am. B **17**, 1051 (2000).
[35] A. W. Snyder and J. D. Love, *Optical Waveguide Theory* (Chapman and Hall, New York, NY, 1983).
[36] H. A. Haus, *Waves and Fields in Optoelectronics* (Prentice-Hall, Englewood Cliffs, New Jersey, 1984), 1st ed.
[37] H. J. Carmichael, *An Open Systems Approach to Quantum Optics* (Springer-Verlag, Berlin, 1993).
[38] H. J. Carmichael, *Statistical Methods in Quantum Optics I: Master Equations and Fokker-Planck Equations* (Springer-Verlag, Berlin, 2003).
[39] H. J. Kimble, *Structure and Dynamics in Cavity Quantum Electrodynamics* (Academic Press, Boston, 1994), pp. 203–266.
[40] L. A. Lugiato, Prog. Opt. **21**, 69 (1984).
[41] R. J. Thompson, Q. A. Turchette, O. Carnal, and H. J. Kimble, Phys. Rev. A **57**, 3084 (1998).
[42] S. M. Tan, http://www.qo.phy.auckland.ac.nz/qotoolbox.html, 2002.
[43] S. M. Tan, J. Opt. B: Quantum Semiclassical Opt. **1**, 424 (1999).
[44] S. M. Spillane, T. J. Kippenberg, K. J. Vahala, K. W. Goh, E. Wilcut, and H. J. Kimble, Phys. Rev. A **71**, 013817 (2005).
[45] M. Borselli, T. J. Johnson, and O. Painter, Appl. Phys. Lett. **88**, 013114 (2006).
[46] L. C. Andreani, G. Panzarini, and J.-M. Gérard, Phys. Rev. B **60**, 13276 (1999).
[47] M. Bayer and A. Forchel, Phys. Rev. B **65**, 041308(R) (2002).
[48] K. Srinivasan, A. Stintz, S. Krishna, and O. Painter, Phys. Rev. B **72**, 205318 (2005).
[49] S. Mosor, J. Hendrickson, B. C. Richards, J. Sweet, G. Khitrova, H. Gibbs, T. Yoshie, A. Scherer, O. B. Shchekin, and D. G. Deppe, Appl. Phys. Lett. **87**, 141105 (2005).
[50] K. Srinivasan, and O. Painter, Appl. Phys. Lett. **90**, 031114 (2006).
[51] L. Mandel and E. Wolf, *Optical Coherence and Quantum Optics* (Cambridge University Press, Cambridge, United Kingdom, 1995).
[52] P. Michler, A. Kiraz, C. Becher, W. V. Schoenfeld, P. M. Petroff, L. Zhang, E. Hu, and A. Imamoglu, Science **290**, 2282 (2000).
[53] C. Santori, M. Pelton, G. Solomon, Y. Dale, and Y. Yamamoto, Phys. Rev. Lett. **86**, 1502 (2001).
[54] J. McKeever, A. Boca, A. D. Boozer, R. Miller, J. R. Buck, A. Kuzmich, and H. J. Kimble, Science **303**, 1992 (2004).
[55] D. Walls and G. Milburn, *Quantum Optics* (Springer, Berlin, 1994), 1st ed.
[56] C. C. Gerry and J. H. Eberly, Phys. Rev. A **42**, 6805 (1990).
[57] A. Rauschenbeutel, P. Bertet, S. Osnaghi, G. Nogues, M. Brune, J. M. Raimond, and S. Haroche, Phys. Rev. A **64**, 050301(R) (2001).
[58] P. Meystre and M. Zubairy, Phys. Lett. **89A**, 390 (1982).
[59] H. J. Carmichael, Phys. Rev. Lett. **55**, 2790 (1985).
[60] J. R. Kuklinski and J. L. Madajczyk, Phys. Rev. A **37**, 3175 (1988).
[61] H. Nha, Phys. Rev. A **67**, 023801 (2003).
[62] H. J. Carmichael, J. Opt. Soc. Am. B **4**, 1588 (1987).
[63] P. Alsing, D.-S. Guo, and H. J. Carmichael, Phys. Rev. A **45**, 5135 (1992).